JOURNAL OF PETROLOGY | VOLUME 51 | NUMBER 9 | PAGES 1941–1965 | 2010 | doi:10.1093/petrology/egq044

Crystallization Kinetics in Continuous Decompression Experiments: Implications for Interpreting Natural Magma Ascent Processes

CARRIE R. BRUGGER* AND JULIA E. HAMMER

DEPARTMENT OF GEOLOGY AND GEOPHYSICS, UNIVERSITY OF HAWAII MANOA, HONOLULU, HI 96822, USA

RECEIVED MARCH 22, 2009; ACCEPTED JULY 23, 2010

Decompression experiments were performed to study the kinetics of plagioclase crystallization during ascent of hydrous rhyodacite magma. These experiments differ from previous studies in that they employ a continuous, rather than stepwise, pressure–time trajectory. Four series of experiments were performed at rates of 0·5–10 MPa h^{-1}*, corresponding to ascent rates of ~0·007–0·14 m s*$^{-1}$*. Experiments quenched along each decompression path allow snapshot-style monitoring of progressive crystallization. As expected, rates of plagioclase nucleation and growth depend strongly on decompression rate. Regardless of decompression rate, approximately equal volumes of feldspar crystallize during a given decompression interval, even when the observed crystallinity is lower than the equilibrium crystallinity. Apparently, a constant degree of solidification is maintained by a crystallization mechanism striking a shifting balance between nuclei formation and growth of existing crystals. Other key results pertain to the efficacy with which experimental results allow interpretation of the decompression histories of natural rocks. Feldspar microlites do not maintain chemical equilibrium with melt. They are more anorthite-rich than equilibrium plagioclase, suggesting that interpretations of magma ascent processes in nature require comparisons with dynamic rather than static (phase equilibrium) experiments. Although decompression rate is an important element controlling final textures in volcanic rocks, no single compositional or textural parameter uniquely records this rate. Of the criteria examined, microlite number density and morphology are the best indicators of magma decompression rate. Based on a small number of comparisons between continuous and multi-step decompression style at the same time-integrated decompression rate (1 MPa h*$^{-1}$*), decompression path evidently influences crystal texture, with stepwise decompression yielding textures correlative with faster decompression than indicated by the time-integrated decompression rate. Thus, consideration of magma ascent style, in addition to rate, will undoubtedly strengthen the interpretive power of experimental studies for constraining natural magma ascent processes.*

KEY WORDS: *crystal nucleation and growth; feldspar; magma decompression; microlites; textural analysis*

INTRODUCTION

Magma ascent processes are increasingly recognized as controlling the style of volcanic activity, thus explaining the intensity of research on post-eruption indicators of ascent rate. For example, the rate at which magma ascends from a storage zone has been estimated using a number of techniques, including seismicity during eruptive periods (Scandone & Malone, 1985; Lees & Crosson, 1989; Endo *et al.*, 1990), plagioclase size distributions (Cashman, 1988, 1992), and reaction rim development on amphibole phenocrysts (Rutherford & Hill, 1993; Rutherford & Devine, 1997). A magmatic closure pressure, or pressure at which kinetic factors inhibit further crystallization and melt chemistry is frozen-in, has been identified in natural volcanic rocks from elevated volatile contents (Newman *et al.*, 1988; Blundy & Cashman, 2008; Castro & Gardner, 2008). Laboratory decompression experiments performed on hydrous magmas of intermediate composition demonstrate that feldspar abundance, composition, and morphology depend on the decompression path, degree of mineral supersaturation, and viscosity of the melt

---

*Corresponding author. Telephone: (808) 956-9544. Fax: (808) 956-5512. E-mail: brugger@hawaii.edu

(Hammer & Rutherford, 2002), thus suggesting that ascent processes are recorded in crystal textures. Decompression drives crystallization because declining H_2O solubility causes volatile exsolution (Burnham & Davis, 1971; Moore *et al.*, 1998; Papale *et al.*, 2006), and subsequent increases in the temperature at which mineral phases form (Wilson *et al.*, 1980; Eichelberger, 1995). Moreover, experiments demonstrate that natural groundmass textures form on eruptive timescales (Geschwind & Rutherford, 1995; Hammer & Rutherford, 2002). The provisional success of the experimental approach for addressing crystallization processes during eruptive decompression suggests that quantitative constraints on the ascent histories of erupted magma may be gleaned ultimately from the groundmass textures of natural rocks (Cashman & Blundy, 2000).

Although the exact nature of magma ascent is not understood, it probably displays temporal and spatial variability between volcanic systems. Magma ascent may at times be intermittent and pulsatory, with rapid accelerations followed by irregular pauses, whereas at other times it may consist of steady fluid flow. The only previous experiments to employ continuous decompression have imposed very rapid decompression (typically >50 MPa h^{-1}) using a manually operated bleed valve, and they have primarily focused on studies of volatile exsolution, bubble nucleation, and bubble growth processes (e.g. Gardner *et al.*, 1999; Mangan & Sisson, 2000; Martel & Schmidt, 2003). Ascent rates of this magnitude correspond to intense explosive eruptions, which typically produce microlite-free materials because the timescales are too short for appreciable groundmass crystallization. In contrast, crystallization in ascending silica-rich magmas, whether natural or synthetic, requires timescales of days to weeks (Rutherford & Gardner, 2000; Martel & Schmidt, 2003). Out of necessity, nearly all decompression-induced crystallization experiments have utilized a stepped technique, either single-step decompression (SSD) or multi-step decompression (MSD) (e.g. Hammer & Rutherford, 2002; Couch *et al.*, 2003*b*; Martel & Schmidt, 2003). In SSD experiments, the pressure is changed manually and instantaneously using a pressure bleed valve from an initial pressure (P_i) to a final pressure (P_f), held at P_f for a period of time, and then quenched. Using variable run times at P_f, this type of experiment can be used to study the evolution of magma in response to a pressure perturbation. In addition, this method provides the only means of applying a known degree of effective undercooling to the sample, and thus it is preferred for placing crystal nucleation and growth rate kinetics in a theoretical context (Hammer, 2004, 2008). However, SSD experiments do not simulate the natural magma ascent process. MSD experiments, which consist of a series of small pressure drops and dwell periods, have been used to study syn-eruptive crystallization and make interpretations about magma ascent rates at various volcanic centers (Hammer & Rutherford, 2002; Coombs *et al.*, 2003; Couch *et al.*, 2003*b*; Martel & Schmidt, 2003; Nicholis & Rutherford, 2004; Browne & Gardner, 2006; Szramek *et al.*, 2006; Suzuki *et al.*, 2007; Castro & Gardner, 2008). The MSD approach is thought to closely approximate natural magma ascent because the small steps in pressure are regarded as insignificant in comparison with the total amount of decompression. However, the effects of varying pressure- and time-step size on resulting crystal textures has never been investigated. Comparisons between stepped and continuous experiments at the same time-integrated decompression rate allow preliminary evaluation of the effects of decompression style on crystal textures.

Here we report the results of continuous decompression experiments performed in a new hydraulically driven screw pump pressure variator with programmable controller. This instrument was designed (Harwood Engineering, Walpole, MA) to measure and control pressure to within a 0·5 MPa tolerance over a 0–300 MPa pressure range using a motorized screw jack that drives a piston out of a large-capacity pressure vessel. The objectives of this research are to (1) examine the evolution of crystal textures during continuous decompression (CD) of H_2O-saturated rhyodacite magma, (2) quantify the effect of decompression rate on crystal texture and phase compositions, and (3) evaluate any differences between continuous and multi-step decompression experimental methods using a small number of pilot experiments. We also evaluate the degree to which chemical equilibrium is reached in each run product, to determine whether any ascent histories promote crystal–melt equilibrium or, conversely, preclude attainment of equilibrium. Experimental results are compared with prior work and a calculated equilibrium liquid line of descent, and we consider plagioclase–melt equilibria in the context of binary T–X phase relations. We conclude with cautionary remarks regarding the interpretation of magma decompression rate from groundmass crystal textures.

METHODS

Starting material

The experimental starting material consists of lightly crushed pyroclasts from the 3430 a BP caldera-forming ignimbrite of Aniakchak volcano in the Aleutian Arc (Table 1, Fig. 1). The experiments are considered germane to crystallization in natural H_2O-rich evolved silicic magmas from a variety of volcanic settings because the kinetics of crystallization in hydrous rhyodacites at the experimental temperature (880°C) should be similar. That is, the present study is relevant to groundmass crystallization in less-evolved natural magmas—andesites and dacites—possessing a rhyodacite matrix melt composition. The starting material is unaltered and contains very few

Table 1: Bulk chemical composition of Aniakchak rhyodacite starting material, wt%

SiO_2	TiO_2	Al_2O_3	FeO_t	MnO	MgO	CaO	Na_2O	K_2O	P_2O_5
71·11	0·56	15·76	2·69	0·15	0·53	2·16	5·69	2·99	0·12

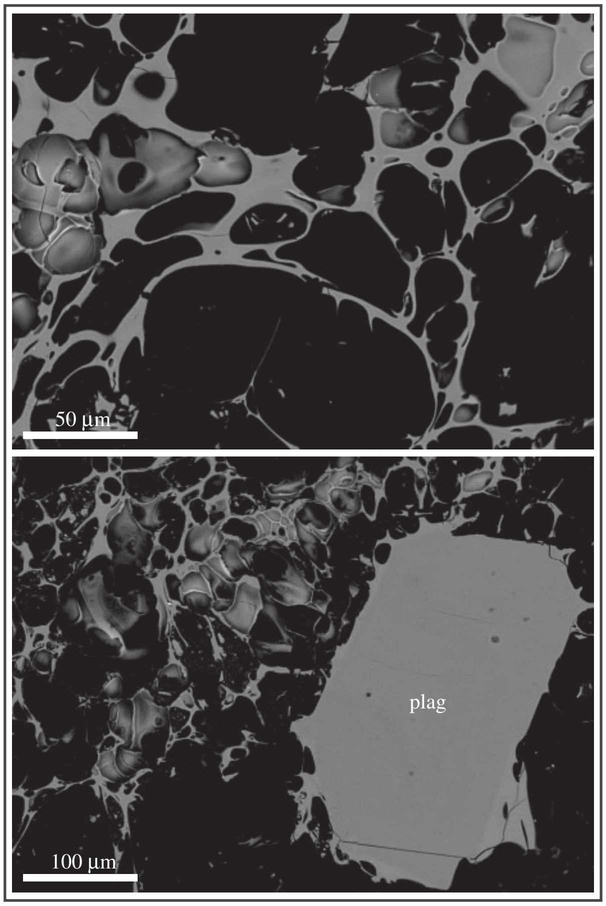

Fig. 1. Backscatter electron images of the Aniakchak Volcano pumice used as a starting material for decompression experiments. This rock contains very few phenocrysts (~2 vol. %) and no plagioclase crystals in the size range created in these experiments (≤100 μm). Void space is black and glass is gray. The lower image shows a typical plagioclase phenocryst (plag), which is slightly darker gray than the glass.

crystals (~2 vol. % phenocrysts and no microlites; Dreher *et al.*, 2005) compared with other similarly prepared natural starting materials (e.g. Hammer & Rutherford, 2002), which reduces the problems of (1) determining which crystals nucleate during an experiment and which crystals are inherited from the starting material, and (2) quantifying the amount of growth on newly formed and pre-existing crystals. The dominant crystallizing phase is plagioclase, the principal focus of textural studies in natural rocks (e.g. Gardner *et al.*, 1998; Hammer *et al.*, 1999, 2000; Cashman & Blundy, 2000; Martel & Poussineau, 2007).

Experimental methods

The initial conditions for decompression experiments were adopted from the pre-eruptive storage conditions determined by Larsen (2006) for this rhyodacite: 870–880°C, oxygen fugacity corresponding to 0·8 ± 0·2 log units above the Ni + NiO (NNO) buffer, and 110–140 MPa. Charges were held at the starting conditions for at least 24 h prior to decompression. The decompression experiments were run H_2O-saturated ($P_{H2O} = P_{TOTAL}$) at a constant temperature of 880°C, initiated from 130 MPa (P_i). Pumice clasts were lightly crushed (rather than powdered) to reduce exposure of phenocryst cores to the matrix melt (Pichavant *et al.*, 2007), with which they are not in equilibrium. The starting material was placed inside $Ag_{70}Pd_{30}$ capsules along with distilled water sufficient to saturate the melt with a vapor at the starting conditions (≥4·3 wt % according to Moore *et al.*, 1998).

Two families of experiments were employed. The first comprised a series of runs quenched at regular pressure intervals along a given decompression path (Table 2). These are termed ‘snapshot’ experiments, because they record the state of the magma at specific pressures during decompression. Interpretations about the evolution of crystal textures through time rest on the assumption that samples decompressed at the same rate follow identical crystallization trajectories. Thus, we infer that a sample quenched at low pressure was previously indistinguishable from a sample quenched at higher pressure. The second family of experiments are called ‘anneal’ experiments because at some point during the decompression they were isolated from the variator and held at a constant pressure for 65–1302 h (Table 2), with the duration contingent on the decompression rate and quench pressure. These anneal durations are similar to or exceed dwell periods used in experimental equilibrium studies at similar temperatures, H_2O contents, and bulk compositions (Rutherford *et al.*, 1985; Hammer *et al.*, 2002; Couch *et al.*, 2003*a*; Larsen, 2006). Chemical equilibrium of anneal samples was evaluated using the time-variance of the matrix glass composition between otherwise identical experiments held at the same final pressure (Tables 2 and 3).

All experiments were run in cold-seal Waspaloy® pressure vessels using methods described in detail previously (Geschwind & Rutherford, 1992; Gardner *et al.*, 1995; Hammer & Rutherford, 2002). Briefly, oxygen fugacity was buffered at the run conditions using a short section of Ni filler rod (~15 mm), temperature was maintained at 880°C using an external thermocouple, and static pressure was applied to the capsules using water as the pressurizing

Table 2: Decompression experiments and results

Sample number	Type	Decompression rate (MPa h^{-1})*	P_f (MPa)	Decompression duration (h)	Time at P_f (h)	N_A (mm^{-2})	ϕ†
6-1	snapshot	10	5	12·6	0	16976 (6179)	0·213 (7)
20-2	snapshot	10	45	8·6	0	9362 (4103)	0·122 (7)
12-2	snapshot	10	68	6·3	0	5732 (2353)	0·077 (5)
5-4	snapshot	10	87	4·4	0	11 (15)	0·001 (0)
12-1	snapshot	10	109	2·2	0	21 (17)	0·003 (1)
6-2	anneal	10	5	12·6	342	16070 (5978)	0·509 (9)
17-3	anneal	10	5	12·6	1302	21053 (846)	0·475 (9)
20-3	anneal	10	26	10·6	219	3029 (1205)	0·283 (7)
5-1	anneal	10	45	8·6	141	301 (89)	0·215 (7)
5-2	anneal	10	87	4·4	90	68 (25)	0·062 (3)
20-1	anneal	10	87	4·4	240	102 (49)	0·083 (4)
18-3	snapshot	2	5	64·9	0	31664 (6481)	0·274 (6)
BJ3	snapshot	2	26	52·9	0	26683 (3367)	0·193 (6)
18-2	snapshot	2	45	44·4	0	17847 (7811)	0·154 (5)
18-1	snapshot	2	68	32·3	0	155 (118)	0·015 (2)
14-2	snapshot	2	87	22·4	0	541 (307)	0·026 (4)
14-1	snapshot	2	109	10·8	0	23 (16)	0·004 (1)
11-1	anneal	2	5	64·9	588	15127 (10815)	0·446 (6)
18-5	anneal	2	45	44·4	94	329 (144)	0·153 (5)
18-4	anneal	2	87	22·3	285	2646 (6435)	0·040 (3)
15-4	snapshot	1	5	134·9	0	347 (49)	0·222 (8)
15-3	snapshot	1	26	111·7	0	1028 (587)	0·156 (6)
15-2	snapshot	1	45	92·4	0	20875 (4191)	0·193 (6)
16-2	snapshot	1	68	66·7	0	7460 (2957)	0·089 (5)
15-1	snapshot	1	87	46·5	0	3809 (1180)	0·032 (4)
16-1	snapshot	1	109	22·5	0	1788 (618)	0·028 (3)
15-7	anneal	1	5	134·9	915	8309 (6518)	0·454 (7)
15-6	anneal	1	45	92·4	813	23074 (9605)	0·225 (6)
15-5	anneal	1	87	46·4	528	14 (27)	0·054 (3)
13-3	snapshot	0·5	5	279·3	0	2510 (593)	0·250 (6)
13-1	snapshot	0·5	26	231·0	0	13708 (3924)	0·203 (7)
8-1	snapshot	0·5	45	197·7	0	6938 (2541)	0·137 (7)
21-1	snapshot	0·5	68	144·0	0	3262 (2117)	0·081 (4)
7-2	snapshot	0·5	87	99·9	0	13586 (6105)	0·088 (5)
7-1	snapshot	0·5	109	48·4	0	15559 (5564)	0·092 (4)
13-2	anneal	0·5	5	279·5	1295	14489 (2642)	0·513 (9)
8-3	anneal	0·5	45	197·8	619	15015 (6866)	0·219 (8)
7-4	anneal	0·5	87	99·9	65	19677 (2441)	0·112 (5)
23-1	anneal	n.a.	130	0·0	–	–	–
23-2	anneal	n.a.	130	0·0	–	–	–
10-4‡	SSD	n.a.	5	0·0	1010	–	–
10-5	SSD	n.a.	45	0·0	966	17909 (7360)	0·225 (6)
10-1	SSD	n.a.	87	0·0	964	4706 (2933)	0·102 (6)
22-2	MSD	1	5	134·2	n.a.	1019 (989)	0·144 (5)
22-1	MSD	1	26	111·6	n.a.	13 (9)	0·004 (2)

*The variator's true decompression rate is slightly faster than the programmed rate shown here.
†In this column the values in parentheses represent 1σ error bars when multiplied by 10^{-3}.
‡Crystals in the 5 MPa SSD experiment are too small to perform textural characterization.
n.a., not applicable.

Table 3: Experimental matrix glass compositions, wt%

Sample	n*	SiO_2†	TiO_2	Al_2O_3	FeO_t	MnO	MgO	CaO	Na_2O	K_2O	P_2O_5	Total
6-1	9	72·29 (87)	0·27 (8)	13·57 (31)	1·19 (6)	0·13 (2)	0·26 (3)	0·61 (9)	5·00 (41)	3·92 (15)	0·07 (5)	97·31
12-3	10	70·92 (72)	0·33 (7)	14·93 (16)	1·56 (13)	0·12 (2)	0·38 (2)	1·58 (5)	5·47 (27)	2·96 (2)	0·06 (3)	98·31
20-2	9	69·56 (115)	0·35 (5)	14·51 (43)	1·29 (12)	0·14 (2)	0·38 (2)	1·32 (28)	5·13 (26)	3·12 (18)	0·06 (4)	95·84
12-2	10	69·14 (52)	0·33 (4)	13·71 (30)	1·49 (12)	0·11 (2)	0·33 (3)	1·18 (18)	5·12 (11)	3·09 (15)	0·02 (2)	94·52
5-4	9	67·95 (68)	0·25 (9)	14·13 (13)	1·83 (11)	0·10 (4)	0·22 (2)	1·46 (5)	5·09 (10)	2·84 (6)	0·02 (2)	93·88
12-1	10	67·06 (45)	0·23 (9)	13·96 (15)	1·60 (10)	0·08 (4)	0·24 (4)	1·42 (4)	5·02 (10)	2·90 (5)	0·01 (1)	92·51
6-2	8	75·29 (105)	0·28 (7)	11·29 (47)	1·36 (13)	0·07 (2)	0·03 (0)	0·20 (5)	3·79 (18)	4·80 (10)	0·07 (4)	97·18
17-3	8	75·42 (85)	0·37 (16)	11·92 (89)	1·32 (46)	0·07 (2)	0·08 (1)	0·28 (5)	3·90 (45)	4·73 (39)	0·03 (2)	98·12
20-3	12	74·19 (102)	0·36 (7)	12·15 (15)	1·29 (4)	0·08 (2)	0·14 (1)	0·51 (9)	4·37 (32)	4·03 (10)	0·06 (6)	97·18
5-1	10	74·31 (113)	0·33 (3)	13·08 (34)	1·22 (8)	0·10 (3)	0·21 (2)	0·74 (14)	3·90 (33)	3·43 (11)	0·07 (9)	97·39
5-2	11	68·78 (44)	0·31 (13)	14·06 (16)	1·61 (14)	0·11 (5)	0·36 (4)	1·48 (13)	5·23 (7)	2·92 (7)	0·04 (3)	94·91
20-1	10	70·95 (53)	0·24 (7)	13·27 (13)	1·07 (9)	0·11 (5)	0·29 (2)	0·98 (7)	4·94 (15)	3·21 (8)	0·02 (3)	95·08
18-3	10	74·67 (93)	0·38 (14)	12·98 (39)	1·38 (18)	0·14 (2)	0·29 (4)	0·35 (5)	4·75 (42)	4·14 (14)	0·05 (3)	99·14
BJ3	10	74·11 (123)	0·32 (7)	12·91 (19)	1·12 (9)	0·11 (3)	0·27 (1)	0·46 (2)	4·43 (21)	3·76 (3)	0·03 (2)	97·53
18-2	8	72·57 (127)	0·32 (11)	13·28 (30)	1·00 (19)	0·11 (2)	0·27 (9)	0·61 (8)	4·20 (29)	3·31 (7)	0·05 (2)	95·71
18-1	6	71·21 (138)	0·39 (8)	14·26 (16)	1·36 (24)	0·12 (1)	0·30 (2)	1·28 (5)	5·15 (25)	3·13 (4)	0·06 (2)	97·24
14-2	10	69·30 (58)	0·33 (10)	13·93 (42)	1·39 (32)	0·08 (2)	0·25 (2)	1·26 (18)	5·16 (12)	3·06 (13)	0·04 (3)	94·80
14-1	10	68·35 (49)	0·32 (6)	13·93 (15)	1·49 (7)	0·10 (4)	0·32 (2)	1·33 (4)	5·13 (8)	2·96 (7)	0·01 (2)	93·94
11-1	8	75·81 (142)	0·36 (7)	11·26 (62)	1·20 (13)	0·06 (2)	0·06 (1)	0·26 (7)	3·83 (35)	4·71 (12)	0·03 (3)	97·59
18-5	9	72·55 (118)	0·35 (9)	13·72 (37)	1·35 (7)	0·11 (3)	0·31 (2)	0·89 (12)	4·43 (22)	3·34 (12)	0·09 (7)	97·14
18-4	11	70·04 (41)	0·33 (5)	13·65 (17)	1·35 (13)	0·12 (3)	0·34 (3)	1·14 (8)	5·04 (9)	3·16 (9)	0·03 (2)	95·20
15-4	9	74·01 (75)	0·34 (5)	13·95 (49)	1·67 (8)	0·15 (2)	0·27 (3)	0·82 (5)	4·77 (32)	3·79 (6)	0·05 (4)	99·83
15-3	10	72·27 (86)	0·35 (8)	13·91 (41)	1·31 (10)	0·14 (2)	0·34 (1)	0·92 (14)	5·30 (12)	3·49 (6)	0·07 (3)	98·10
15-2	7	75·48 (76)	0·32 (6)	13·17 (7)	1·04 (16)	0·10 (3)	0·21 (4)	0·48 (5)	4·19 (20)	3·45 (9)	0·05 (3)	98·50
16-2	10	71·30 (35)	0·41 (8)	13·52 (16)	1·37 (12)	0·09 (4)	0·32 (2)	0·94 (9)	4·96 (13)	3·20 (5)	0·01 (1)	96·12
15-1	10	69·51 (73)	0·34 (7)	14·00 (49)	1·22 (12)	0·10 (3)	0·33 (7)	1·31 (25)	4·94 (17)	3·01 (11)	0·03 (3)	94·79
16-1	10	67·96 (38)	0·32 (6)	13·80 (14)	1·37 (10)	0·12 (2)	0·36 (3)	1·32 (7)	4·97 (9)	3·02 (4)	0·02 (4)	93·25
15-7	11	78·14 (109)	0·33 (5)	11·28 (92)	1·15 (9)	0·05 (2)	0·07 (1)	0·25 (7)	3·63 (33)	4·83 (12)	0·06 (5)	99·81
15-6	10	75·40 (73)	0·27 (9)	12·77 (31)	1·23 (12)	0·09 (2)	0·15 (1)	0·63 (13)	4·47 (21)	3·81 (9)	0·04 (5)	98·85
15-5	10	70·22 (13)	0·37 (7)	13·73 (9)	1·28 (8)	0·08 (3)	0·35 (2)	1·23 (3)	5·07 (9)	3·12 (5)	0·04 (4)	95·49
13-3	11	74·15 (73)	0·32 (5)	12·81 (17)	1·28 (9)	0·09 (2)	0·13 (2)	0·31 (4)	4·47 (33)	4·44 (3)	0·03 (3)	98·03
13-1	10	74·67 (101)	0·33 (5)	12·79 (10)	1·14 (7)	0·11 (2)	0·25 (2)	0·42 (2)	4·69 (25)	3·80 (4)	0·03 (2)	98·24
8-1	10	73·83 (84)	0·31 (6)	13·17 (10)	1·03 (6)	0·13 (2)	0·30 (1)	0·55 (2)	4·67 (30)	3·63 (3)	0·05 (3)	97·66
21-1	10	71·27 (37)	0·43 (4)	13·40 (26)	1·23 (6)	0·13 (3)	0·31 (3)	0·89 (11)	4·88 (11)	3·30 (4)	0·02 (3)	95·85
7-2	8	70·43 (47)	0·31 (6)	13·33 (34)	1·07 (12)	0·09 (4)	0·30 (5)	0·91 (16)	4·90 (16)	3·21 (12)	0·02 (3)	94·57
7-1	10	69·15 (53)	0·23 (12)	13·74 (33)	1·44 (10)	0·09 (3)	0·17 (2)	1·10 (13)	4·96 (9)	3·04 (9)	0·004 (10)	93·92
13-2	6	77·24 (68)	0·31 (5)	10·33 (15)	1·76 (16)	0·07 (2)	0·06 (1)	0·20 (2)	3·14 (26)	4·60 (30)	0·02 (4)	97·73
8-3	10	74·77 (65)	0·27 (7)	12·24 (9)	0·98 (7)	0·08 (3)	0·18 (1)	0·52 (10)	4·44 (16)	3·82 (6)	0·05 (7)	97·36
7-4	5	70·64 (65)	0·26 (6)	13·24 (38)	0·90 (9)	0·07 (1)	0·21 (2)	0·91 (21)	4·78 (12)	3·29 (12)	0·03 (2)	94·31
23-1	9	67·11 (35)	0·45 (6)	14·10 (20)	2·35 (9)	0·12 (3)	0·54 (1)	1·68 (5)	5·09 (9)	2·71 (6)	0·03 (2)	94·18
23-2	10	67·29 (52)	0·43 (7)	14·02 (15)	2·29 (7)	0·13 (3)	0·56 (1)	1·71 (4)	5·12 (8)	2·76 (4)	0·03 (3)	94·35
10-5	10	69·50 (113)	0·36 (7)	12·96 (15)	1·15 (10)	0·08 (3)	0·20 (1)	0·49 (1)	4·58 (26)	4·17 (6)	0·03 (2)	93·53
10-1	8	71·28 (64)	0·32 (5)	13·61 (15)	1·08 (11)	0·12 (1)	0·25 (1)	0·80 (2)	4·64 (37)	3·30 (4)	0·03 (1)	95·42
22-2	11	71·20 (83)	0·38 (8)	15·05 (22)	1·76 (12)	0·15 (1)	0·42 (7)	1·31 (26)	5·34 (37)	3·70 (20)	0·06 (5)	99·39
22-1	8	70·97 (51)	0·42 (5)	15·12 (15)	1·56 (21)	0·15 (3)	0·53 (2)	1·68 (5)	4·90 (26)	3·05 (4)	0·09 (2)	98·48

*Number of microprobe analyses averaged to determine the average glass composition and estimated error.
†Values in parentheses represent 1σ errors when multiplied by 10^{-2}.

medium and monitored using a factory-calibrated Heise gauge providing 0·5 MPa precision. During CD experiments, pressure was controlled to within ±0·5 MPa by the pressure variator, and regularly checked against the Heise gauge. Snapshot experiments were quenched immediately upon reaching their final pressure. When an anneal experiment reached final pressure (P_f) it was isolated from the variator and pressure was checked daily. All experiments were quenched by removing the pressure vessel from the furnace and quickly inverting it so that the charge fell to the water-cooled end (after Mangan & Sisson, 2000), which is estimated to cool samples by 300°C within 6 s.

Continuous decompression (CD) experiments were run at four decompression rates: 0·5, 1, 2, and 10 MPa h^{-1} (Table 2). The slowest decompression rate corresponds to an ascent rate (~0·007 m s^{-1}) typical of a dome-building effusive eruption (e.g. Mount St Helens), whereas the fastest decompression simulates an ascent rate (~0·14 m s^{-1}) corresponding to that preceding low-intensity explosive activity (Rutherford & Gardner, 2000). Along each decompression path, six snapshot experiments and three anneal experiments were performed, with snapshots at 109, 87, 68, 45, 26 and 5 MPa, and anneal runs at 87, 45, and 5 MPa (Table 2). Three single-step decompression (SSD) experiments were performed and quenched at 87, 45 and 5 MPa. In addition, two multi-step decompression (MSD) experiments were conducted using a pressure step of 10 MPa every 10 h, which is equivalent to a time-integrated decompression rate of 1 MPa h^{-1}. The MSD decompression experiments were quenched at 26 and 5 MPa, and performed according to previously published techniques (e.g. Hammer & Rutherford, 2002; Couch *et al.*, 2003*b*; Martel & Schmidt, 2003; Browne & Gardner, 2006; Szramek *et al.*, 2006). Assuming a lithostatic pressure gradient, each 10 MPa pressure step corresponds to instantaneous ascent of ~300 m. Most MSD experiments designed to study decompression-induced crystallization utilize time steps longer than 10 h. Some of the MSD experiments performed by Martel & Schmidt (2003) had step sizes between 1 day and 15 s, although these comparatively short experiments do not result in significant crystallization, and are therefore used to study water exsolution and bubble growth.

Timescales of decompression-induced water migration from silicate melts into bubbles occurs much faster than the decompression timescales used in CD experiments (Zhang *et al.*, 1991; Zhang & Behrens, 2000). Previous experimental and analytical work (Gardner *et al.*, 1999; Martel & Schmidt, 2003) suggests that melt–bubble equilibrium is maintained with respect to H_2O distribution for the decompression rates utilized here. Thus, differences in crystal contents and textures observed in CD experiments at a given pressure result only from factors influencing the kinetics of crystallization, not factors controlling H_2O migration. Although the single pressure steps in MSD experiments are nearly instantaneous and thus significantly faster than rates of H_2O exsolution, the anneal period between pressure steps is sufficient for attainment of melt–bubble equilibrium before the next pressure drop.

Analytical methods

Chemical compositions were obtained using a Cameca SX-50 electron probe microanalyzer (EPMA) at University of Hawaii Manoa and a Cameca SX-100 EPMA at the University of Oregon. Glass compositions were analyzed using a 15 kV accelerating voltage, 10 nA beam current, and defocused spot size of 5–20 μm (Table 3). Sodium and potassium were measured first to minimize loss owing to volatilization, and were extrapolated back to initial (time = 0) values using the online correction scheme of Nielsen & Sigurdsson (1981). A suite of synthetic hydrated glasses provided by M. J. Rutherford (described by Devine *et al.*, 1995) were used as bench standards (e.g. Hammer & Rutherford, 2002) to derive nominal correction factors to account for alkali loss in the hydrous glasses (Devine *et al.*, 1995; Morgan & London, 1996). Crystalline phases were analyzed similarly, except using a focused beam. Microlite crystals were not detectably zoned with respect to back-scattered electron (BSE) generation, and small size precluded multiple analyses per grain. Therefore all reported compositions were obtained using a focused beam on the crystal centers. Many charges contained crystals too small to analyze quantitatively, and thus the reported analyses are biased toward crystals larger than ~5 μm. Transect analyses were performed on several suitably sized crystals, yielding compositional variation smaller than the intra-grain variation within the same sample. The raw data were corrected using ZAF-PAP procedures (e.g. Reed, 1993). Chemical compositions reported in Table 3 are averages of 5–12 analyses from each sample.

BSE images were collected with a JEOL-5900LV scanning electron microscope (SEM) at University of Hawaii Manoa using an acceleration voltage of 15 kV. Although container-initiated crystallization was not observed, images were acquired away from the sample edges whenever possible. Most quantitative textural measurements utilized images at 750× magnification; however, samples containing fewer and/or larger crystals were imaged at 500× and 250×. Between four and 15 images from each sample were analyzed, with quantity depending on the homogeneity of the sample and the area density of crystals. Plagioclase microlite number density (crystals mm^{-2}, N_A) on a vesicle-free basis was obtained using methods described by Hammer *et al.* (1999) using the image processing software package ImageJ. One standard deviation error bars were calculated using the variance between images. The area fraction of plagioclase microlites (ϕ_A) on a vesicle-free basis was determined using a method similar to that of Hammer *et al.* (1999), except that a point counting grid was utilized, and error bars were determined using the Van der Plas & Tobi (1965) equation for determining point counting errors, $\{[\phi_A\ (\phi_A - 1)]/n\}^{1/2}$, where n is the number of points counted. Because the samples contain no discernible fabric, the area fraction of plagioclase microlites (ϕ_A) is assumed equal to the volume fraction (ϕ; DeHoff & Rhines, 1968). Phenocrysts inherited from the starting material are significantly larger (>200 μm) than experimentally produced crystals (≤100 μm), thus exclusion of phenocrysts from textural analyses was straightforward. Only plagioclase crystals formed during experiments were used to determine microlite number density and area fraction. Based on five repeat experiments at different decompression rates and quench pressures, we determined that N_A and ϕ are experimentally reproducible within the 1σ error associated with the variation between images of a single sample. In other words, variation within a sample exceeds variation between repeat experiments.

Microlite number density and area fraction measurements were used to calculate the characteristic crystal size, S_N (mm) $= (\phi_A/N_A)^{1/2}$, and volumetric number density, N_V (mm^{-3}) $= N_A/S_N$ (Cheng & Lemlich, 1983; Blundy & Cashman, 2008). Crystal nucleation rates (I, in mm^{-3} s^{-1}) and growth rates (G, in mm s^{-1}) were calculated using

$$I = \frac{N_V}{t} \tag{1}$$

$$G = \frac{S_N}{t} = \left(\frac{\phi_A}{N_A}\right)^{1/2} \Big/ t \tag{2}$$

respectively, where t is the total amount of time spent below P_i (Hammer & Rutherford, 2002). The nucleation rates thus obtained are time-integrated values and are lower than would be observed immediately following a nucleation pulse. Similarly, actual instantaneous crystal growth rates are higher than are obtained using equation (2), given that linear growth rates are highest for small crystals and thus greatest following a nucleation pulse. We also emphasize that the G values obtained using equation (2) are based on the characteristic size of a population and do not represent growth rates observed for any single crystals.

A small amount of plagioclase crystallization (totalling ~1·6 vol. %) occurred within 24 h at 130 MPa and 880°C, the conditions imposed on all experiments prior to decompression. These 'initial dwell' crystals exhibit a limited size range (20–60 μm at 130 MPa, increasing to ≤100 μm at $P_f = 5$ MPa), which makes them distinctly larger than decompression-induced nucleated crystals and smaller than phenocrysts inherited from the starting material (>200 μm; Fig. 1). Crystal size distribution analyses of these experimental charges (Brugger & Hammer, 2010) confirm the visual size distinction between dwell and decompression-induced crystals. Crystallization during the initial dwell period suggests that either (1) the magma storage conditions prior to the 3430 a BP caldera-forming Aniakchak eruption are not exactly 130 MPa and 880°C, or (2) the natural magma was initially slightly H_2O-undersaturated, as suggested by Larsen (2006). Because this study does not address the magma ascent history specific to the 3430 a BP Aniakchak eruption, the mismatch between the magma chamber conditions and the experimental starting conditions is not relevant. Rather, the fact that each experiment was preceded by a dwell period of identical conditions ensures that results are internally consistent. To ensure that our interpretations of decompression-induced crystallization are not affected by the crystals formed at P_i or crystal growth that occurred prior to commencement of decompression, the average microlite number density (N_A) and area fraction (ϕ) of feldspar (72 mm^{-2} and 0·016, respectively) in samples quenched after 24–40 h at P_i were subtracted from quantitative textural results (Table 2).

RESULTS

Mineralogy

Every charge contains plagioclase, orthopyroxene, clinopyroxene, Fe–Ti oxides, and trace amounts of apatite. Alkali feldspar is present only in anneal runs terminated at low pressure (26 and 5 MPa). A silica phase formed in anneal experiments at 5 MPa. Distinctive botryoidal texture, multiple contraction fractures, and preferential formation at the margins of irregular void spaces all suggest cristobalite deposition from a late-stage, silica-rich vapor phase (Hoblitt & Harmon, 1993). No silica phase is present in snapshot experiments at any of the quench pressures in this study, suggesting a delay in nucleation longer than the timescale of the slowest decompression run to 5 MPa. Although amphibole should be stable at 880°C and 109 MPa as determined by Larsen (2006), it was not present as a groundmass phase in the runs at $P_f = 109$ MPa. However, this is not surprising because the starting material contained only trace amounts of amphibole (Dreher *et al.*, 2005) and these conditions are very close to the amphibole stability curve (Larsen, 2006).

At each quench pressure, all slowly decompressed samples (≤1 MPa h^{-1}) contain microlites that formed during decompression, in addition to initial dwell crystals. In the two fastest decompression series (10 and 2 MPa h^{-1}), microlites resulting from decompression-induced nucleation are not visible until ≤68 MPa (Fig. 2c and d). A nucleation delay following exposure of a melt to conditions of crystal supersaturation is commonly observed in silicate systems (James, 1974, 1985; Fokin *et al.*, 1981), and attributed to the time necessary for structural reorganization of the melt

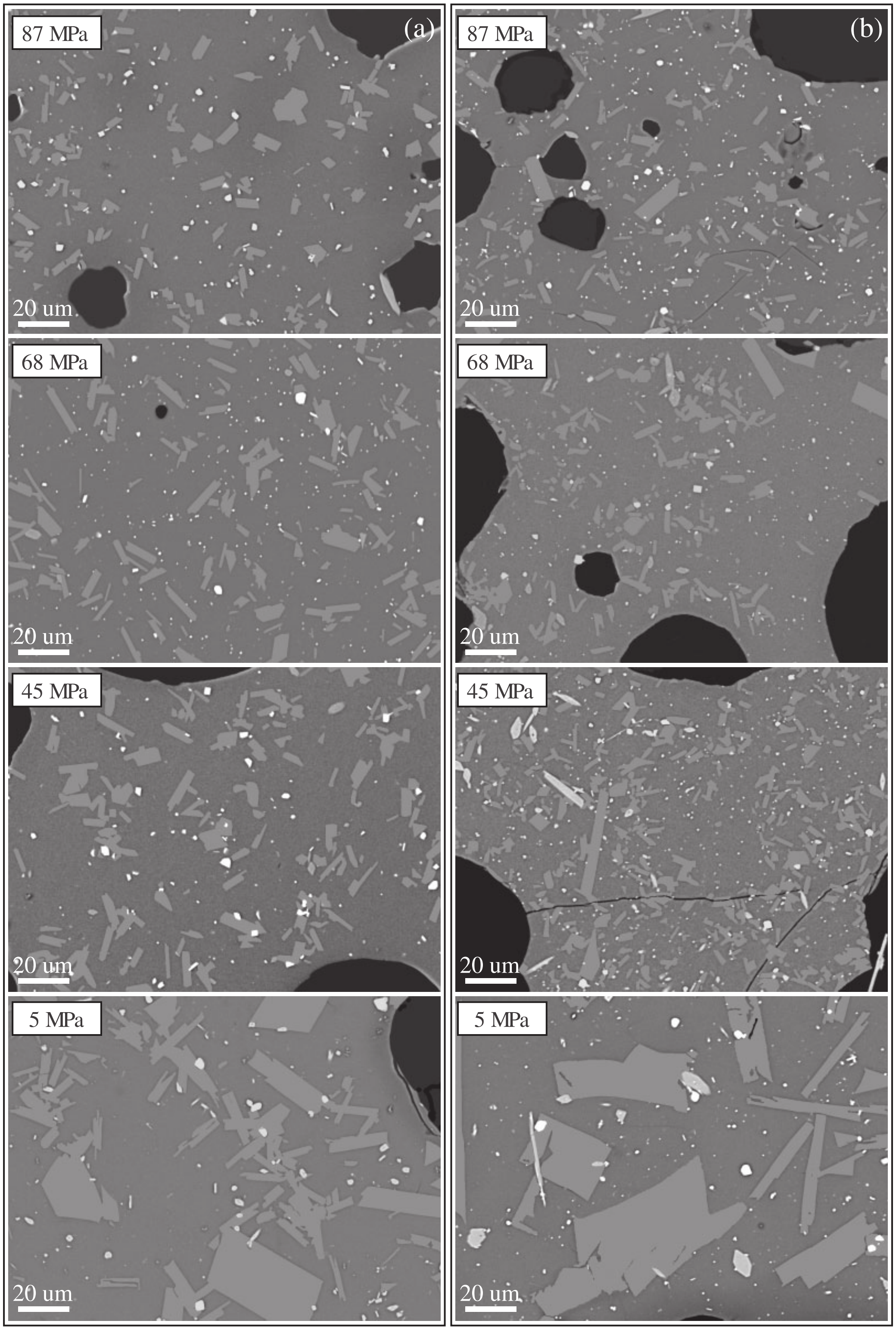

Fig. 2. Backscatter electron images of textures found in snapshot samples: (a) 0·5 MPa h^{-1}; (b) 1 MPa h^{-1}; (c) 2 MPa h^{-1}; (d) 10 MPa h^{-1}. Feldspar crystals (medium gray) have been manually colored a lighter shade of gray to make viewing easier. Black areas are void space, white grains are Fe–Ti oxides, and light gray crystals are pyroxene or occasionally apatite. The different scale for the 87 MPa runs in (c) and (d) should be noted; all crystals in these two runs are inherited from the initial dwell period.

(continued)

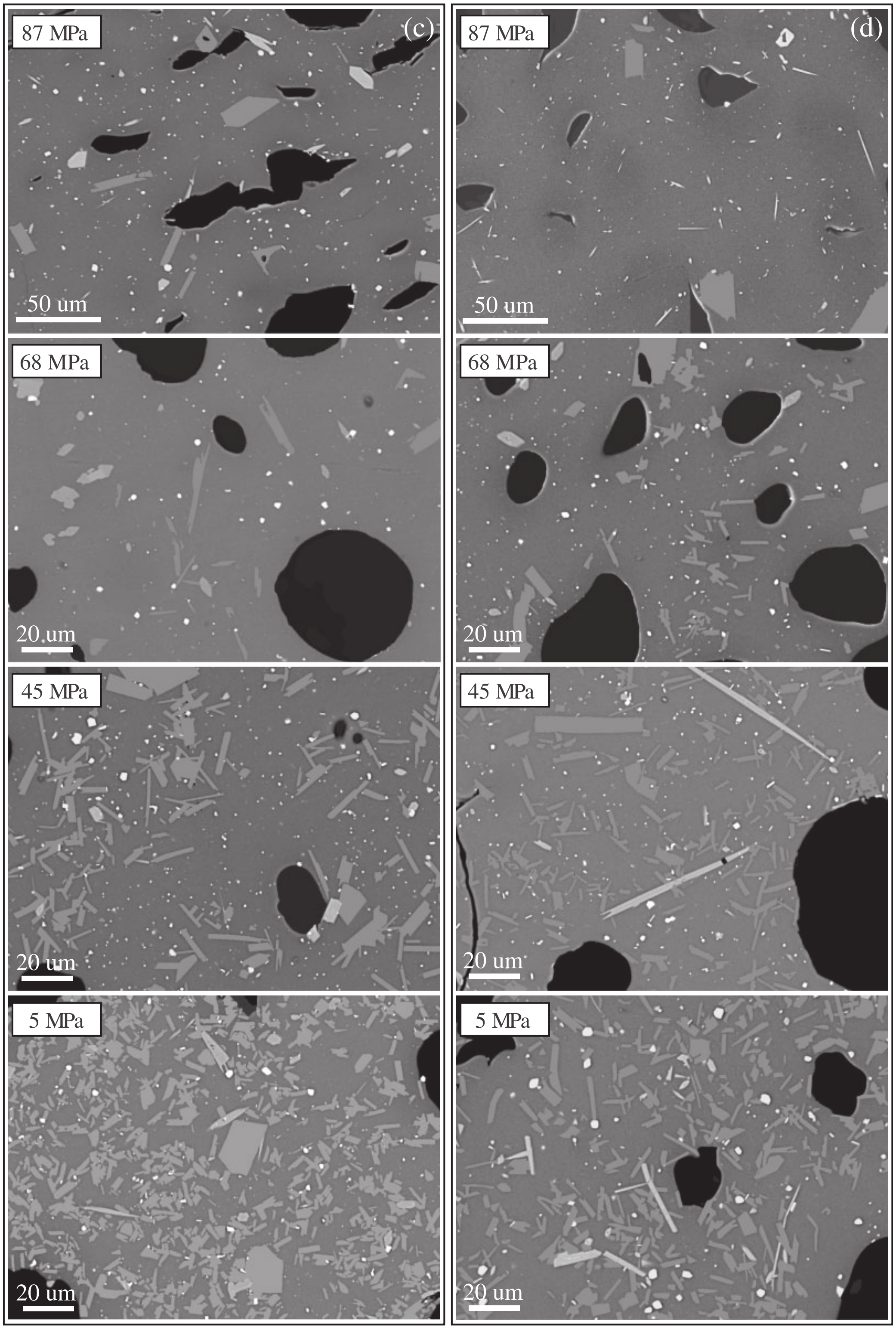

Fig. 2. Continued.

and establishment of subcritical clusters. The lack of decompression-induced nucleation in rapidly decompressed (≥ 2 MPa h^{-1}) rhyodacite quenched at ≥ 87 MPa suggests a feldspar nucleation delay of the order of $\sim 4{\cdot}5$–6 h for the 10 MPa h^{-1} decompression rate and ~ 11–22 h for 2 MPa h^{-1}. The presence of decompression crystals in every slowly decompressed sample constrains plagioclase nucleation delays of <22 h in the 1 MPa h^{-1} series and <49 h in the 0·5 MPa h^{-1} series (Table 2).

Crystal morphology

Fe–Ti oxide crystals are typically equant, euhedral, small (<5 μm), and evenly distributed throughout the sample. Although Fe–Ti oxide crystals range up to 20 μm in some samples, there is no systematic correlation between oxide size and decompression rate or quench pressure. Pyroxene crystals are generally euhedral, with the exception being hopper and elongate (40–60 μm) skeletal crystals in runs decompressed at >0·5 MPa h^{-1} and annealed at 5 MPa, and those annealed at 26 MPa following decompression at 10 MPa h^{-1}. Pyroxene crystals are generally <20 μm in length and <10 μm in width, as ascertained from BSE images. However, some samples contain crystals of similar width ranging up to 60 μm in length. Pyroxene crystal length is uncorrelated with decompression rate or quench pressure, suggesting that high aspect ratio crystals are simply slices through highly flattened tabular morphologies (Peterson, 1996).

Feldspar crystallization is extremely sensitive to changes in P_{H_2O} and effective undercooling; consequently, feldspar textures vary coherently with respect to the experimental variables of decompression rate and quench pressure (Fig. 2; and Electronic Appendix 1, available for downloading at http://www.petrology.oxfordjournals.org). Qualitative inspection of samples at each quench pressure indicate that feldspar morphologies (excluding initial dwell crystals) display progressively more disequilibrium features as decompression rate increases. Slowly decompressed samples contain predominantly tabular and euhedral plagioclase crystals during almost the entire decompression history, with a small fraction of swallowtail morphologies present in only the lowest pressure sample (Fig. 2a). As decompression rate increases, swallowtail and high aspect ratio crystals become more prevalent and they begin appearing at progressively higher quench pressures (Fig. 2b–d). Crystal populations also display distinct trends attributable to decompression rate. At the highest pressures examined, fast decompression leads to growth of initial dwell crystals and the absence of nucleation, resulting in few large crystals; slow decompression is characterized by early nucleation as well as growth, which results in a crystal population dominated by small microlites (Fig. 2, top row). By the time low pressures are reached, rapid decompression causes substantial nucleation, which results in a large number of small crystals. Slowly decompressed samples ultimately contain fewer and larger crystals as a consequence of growth-dominated crystallization (Fig. 2, bottom row).

Crystals in anneal runs are typically larger than crystals in snapshot runs at the same decompression rate and quench pressure (Fig. 3). However, the textures of anneal samples quenched at the same P_f are not homogeneous. Anhedral morphologies and disequilibrium textures are commonly found in samples quenched at low pressures and with faster initial decompression rates (Fig. 3). The textural variation between samples 17-3 and 6-2, both decompressed at 10 MPa h^{-1} to $P_f = 5$ MPa, suggests that the length of the anneal segment is crucial to the textural development of the crystals. Although the volume of plagioclase in these samples is identical, the sample with longer anneal time (sample 17-3; 1302 h) contains euhedral crystals whereas the shorter duration experiment (sample 6-2; 342 h) contains crystals with disequilibrium textures (swallowtail and hopper crystals).

Skeletal and hopper morphologies are common in the multi-step decompression experiments, whereas comparable continuous decompression experiments contain dominantly faceted crystals (Fig. 4). Another interesting textural difference between CD and MSD samples is inhomogeneous distribution of plagioclase crystals in the MSD runs. Crystal-free pockets are interspersed with areas containing a high density of contiguous or clumped crystals. These grains may touch outside the plane of the thin section.

Phase compositions

Glass

Anneal experiments performed at different decompression rates and for various anneal durations produce comparable matrix glass compositions and similar volumes of plagioclase at each quench pressure with no apparent relationship to decompression rate or anneal duration (Tables 2 and 3). This time-invariance suggests that the anneal runs achieved chemical steady state, and thus are interpreted as achieving equilibrium plagioclase compositions, crystallinities, and glass compositions. Matrix glasses of anneal experiments thus record the equilibrium liquid line of descent during isothermal crystallization at varying P_{H_2O}. With the exception of alkali feldspar (which forms only in low-pressure anneal runs), potassium is essentially incompatible in the crystallizing assemblage. Thus the K_2O content of snapshot glasses increases with total crystallinity (Fig. 5). Similarly, as plagioclase is the only crystallizing phase rich in aluminum, progressive decline in glass Al_2O_3 isolates the plagioclase contribution to the crystallizing assemblage (Fig. 5).

The K_2O contents of matrix glass in snapshot experiments reveal the extent of crystallization driven by

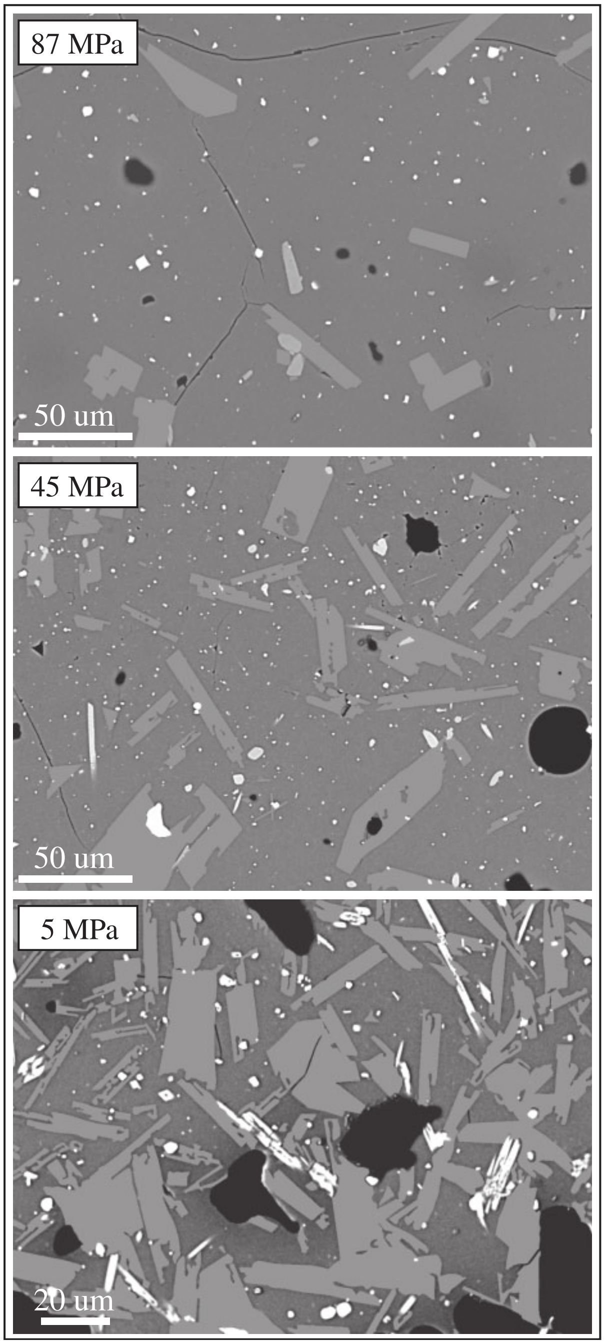

Fig. 3. Textural examples of anneal runs at 87, 45, and 5 MPa. The samples shown were decompressed at 2 MPa h^{-1}, and annealed for 285, 94, and 588 h, respectively. Textural examples of snapshot runs from the same decompression series are shown in Fig. 2c. Feldspar crystals (medium gray) have been manually colored to make viewing easier. Black areas are void space, white grains are Fe–Ti oxides, and light gray crystals are pyroxene.

continuous and multi-step decompression, with the K_2O contents of anneal experiments providing equilibrium values for comparison. At 109 MPa, each snapshot run contains glass with nearly the same K_2O content as the interpolated anneal run using bracketing experiments at 130 and 87 MPa. This indicates not only that the extent of crystallization at pressures $\geq$109 MPa is equivalent regardless of decompression rate in the investigated range, but also that crystallization occurs sufficiently rapidly to maintain chemical equilibrium (Fig. 5). Upon further decompression, the snapshot runs systematically depart from the equilibrium K_2O–P_f trend. Across all P_f values, snapshot runs performed at the lowest decompression rate have compositions that most closely approach equilibrium, although the high Al_2O_3 contents of the slowest-decompressed samples suggest disproportionate contributions from pyroxene and other nominally Al-free phases to the total crystallinity. Conversely, high decompression rate and MSD produce glasses that are markedly low in K_2O, indicating insufficient crystallization relative to equilibrium. Because the anneal runs at the lowest pressures (5 and 26 MPa) contain alkali feldspar containing up to 4 wt% K_2O, the potassium contents of the glasses in these runs are lower than would be the case if potassium behaved incompatibly. Thus the alkali feldspar-free snapshot runs are even further from the equilibrium crystal content than is suggested by their glass K_2O contents.

Plagioclase

Plagioclase compositions vary widely among the 4–15 crystals analyzed in each run (Fig. 6, Table 4, and Supplementary Data Table 1, available at http://www.petrology.oxfordjournals.org), and there is no clear relationship between crystal size and composition. The compositions in snapshot experiments vary by *c.* 10–15 mol% An at each P_f, and there appears to be no relationship between decompression rate and plagioclase composition (Fig. 6a and b). Anneal experiments display variation over a similarly wide range, although the 5 MPa samples contain some crystals with more Ab- and Or-rich compositions (Fig. 6c). The most An-rich crystals in all snapshot and anneal runs have similar compositions (An_{39-43}), regardless of decompression rate or quench pressure. In anneal samples, the compositions of the most alkalic crystals vary coherently with P_f. Samples quenched at 87 and 45 MPa contain crystals with $Or_{\leq 3\cdot 9}$, and anorthite contents of $\geq$27·9 and $\geq$21·1, respectively. In contrast, crystals in $P_f = 5$ MPa samples are $An_{\geq 5\cdot 6}$ and up to $Or_{25\cdot 5}$.

Plagioclase volume fraction and microlite number density

Plagioclase volume fractions (ϕ) in anneal experiments are consistent with the K_2O trends described above; they exhibit an accelerating increase in crystallinity with decreasing P_f (Table 2 and Fig. 7a). As with the compositional data, ϕ values for anneal samples provide a means of evaluating the extent to which snapshot crystallinities

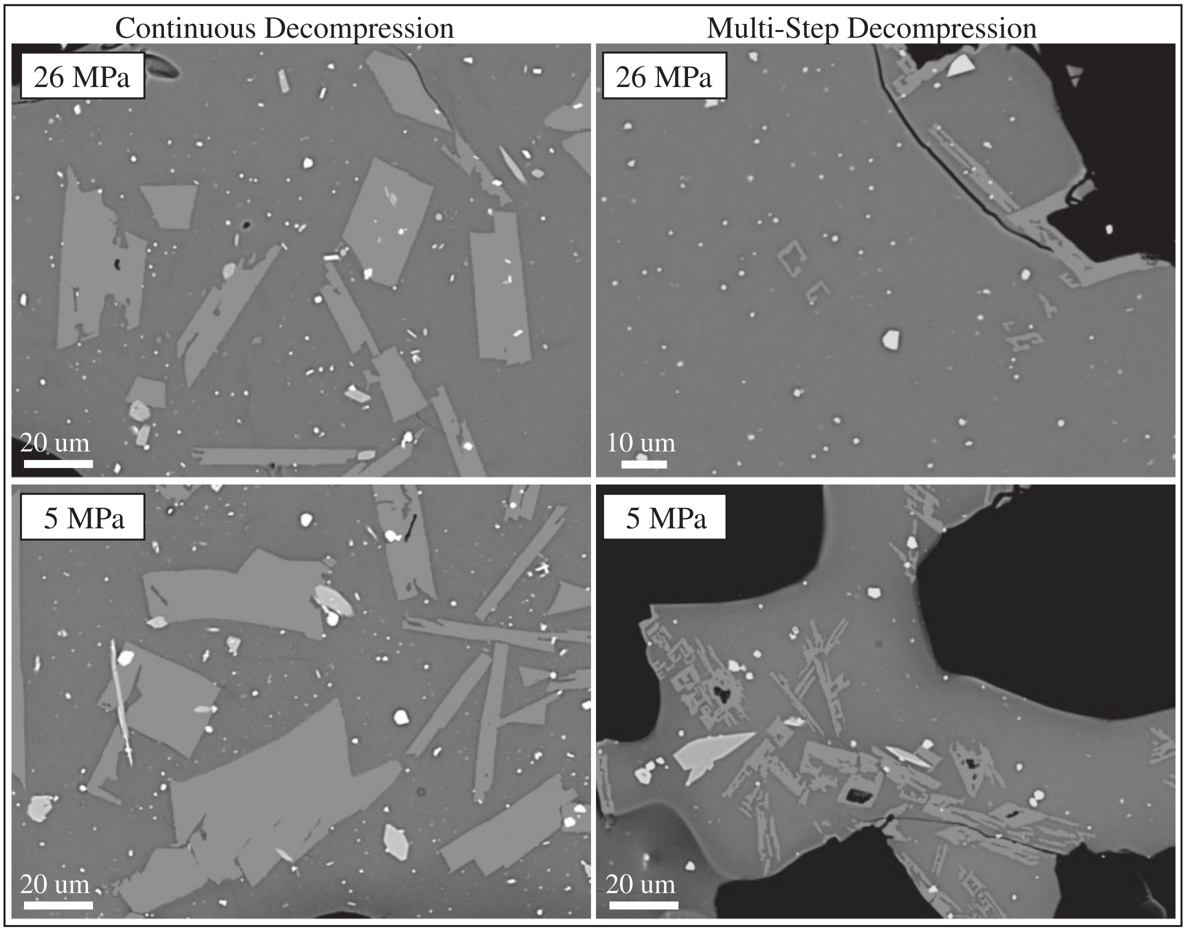

Fig. 4. Textural comparisons between continuous decompression and multi-step decompression experiments, both at an integrated decompression rate of 1 MPa h^{-1}. Feldspar crystals (medium gray) have been manually colored to make viewing easier. Other phases include pyroxene (light gray) and Fe–Ti oxides (white). Black areas are void space.

approach equilibrium. Snapshot ϕ values are surprisingly uncorrelated with decompression rate, having nearly uniform feldspar contents for each P_f and very few outliers.

At the highest pressures, ϕ values in snapshot experiments are within 2σ of the anneal values. However, starting at ~45 MPa, the snapshot ϕ values progressively fall below the anneal values. By 5 MPa, the snapshot runs contain approximately half the amount of plagioclase present in anneal samples. Thus, the volume fraction of plagioclase obtained by image analysis is consistent with glass composition data, which reveal progressive departure from equilibrium with decreasing P_f.

At each of the pressures examined, multi-step decompression produces significantly less plagioclase than continuous decompression (Fig. 7a). By 26 MPa the MSD sample crystallized less than 2% plagioclase, approximately equivalent to the CD sample at 87–109 MPa, and by 5 MPa it contains only 16% plagioclase, which was present in the CD experiment by 45 MPa. This is consistent with previous studies that recognize groundmass crystallinities in near-fully decompressed MSD samples to be several vol. % lower than in natural samples (Hammer & Rutherford, 2002; Couch *et al.*, 2003*b*; Cashman & McConnell, 2005).

In contrast to ϕ, microlite number density (N_A) varies appreciably as a function of decompression rate between CD snapshot samples (Fig. 7b). At the two fastest decompression rates, N_A remains fairly low until $\leq$50 MPa, then peaks at 5 MPa. At an intermediate decompression rate of 1 MPa h^{-1}, N_A increases to a peak at 45 MPa, and then declines. There is no obvious number density peak at the slowest decompression rate. Rather, moderately high N_A is achieved at relatively high pressure (by 109 MPa) and subsequent snapshots in this series have similar or lower N_A values.

Textural differences between the products of high-intensity and low-intensity volcanic eruptions are manifested in the relative magnitudes of N_A and ϕ (Fig. 8),

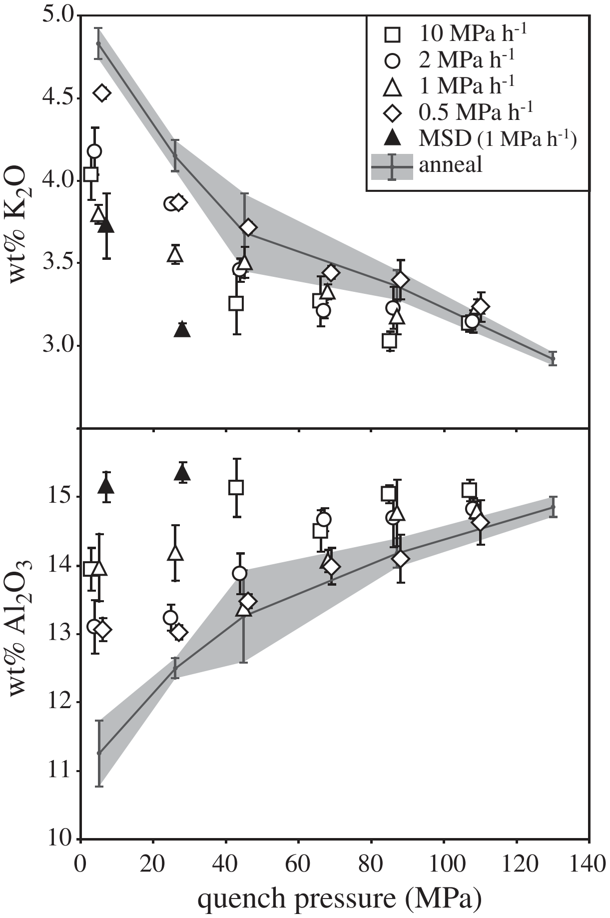

Fig. 5. Variation of glass compositions in MSD samples and CD snapshot samples compared with anneal samples. Each point is an average of 5–12 microprobe analyses and error bars represent 1σ variation. The anneal curve was created by averaging all the anneal runs at the given quench pressure and the shading around the curve represents this variation between anneal experiments at the same pressure. Each decompression series is offset slightly on the *x*-axis for clarity.

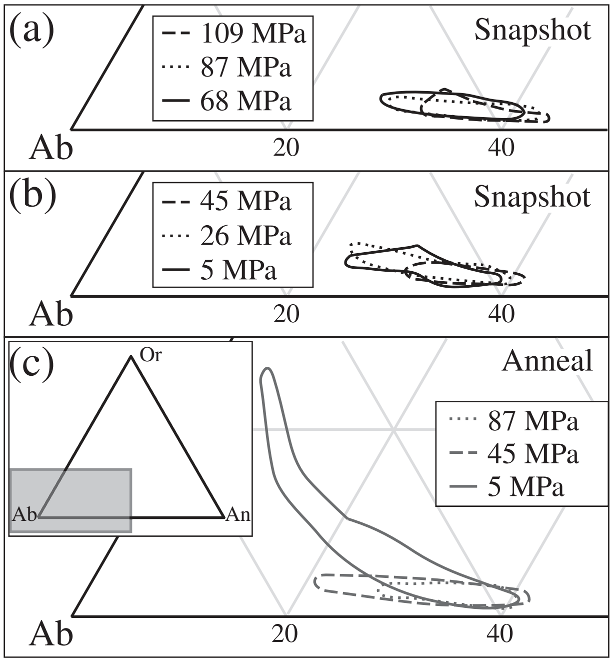

Fig. 6. Feldspar microlite compositions are plotted in the Anorthite–Albite–Orthoclase (An–Ab–Or) ternary diagram. For clarity, plots are separated into three groups: (a) high-pressure snapshot; (b) low-pressure snapshot; (c) anneal samples. Each field represents a different quench pressure, with no distinction made between different decompression rates. The plot area in (c) is represented by the shaded region in the inset.

textural parameters that therefore facilitate quantitative comparisons of experimental products and natural volcanic rocks. The 1991 pre-climactic subplinian eruptions of Mt. Pinatubo and 1980 post-climactic subplinian eruptions of Mount St Helens produced pyroclasts with high number densities but low total volume fraction (Hammer *et al.*, 1999; Cashman & McConnell, 2005). In contrast, the effusive 1986–1995 dome-building eruptions of Merapi, 1991–1995 block-and-ash flows of Mt. Unzen, 1997 vulcanian explosions at Soufrière Hills, and 1859 lava flows from Mauna Loa Volcano generated samples with low N_A values but high plagioclase volume fractions (Hammer *et al.*, 2000; Clarke *et al.*, 2007; Noguchi *et al.*, 2008; Riker *et al.*, 2009). The experimental samples of this study plot within the range of effusive and low-intensity explosive eruptions, consistent with the decompression rates utilized. The coincidence of N_A/ϕ between synthetic and natural samples supports the underlying premise of our study—that the texture-controlling processes of crystallization can be reproduced in a laboratory environment.

Nucleation and growth rates

As expected from the above trends in ϕ and N_A, plagioclase nucleation (I) and growth rates (G) in snapshot experiments vary with decompression rate and quench pressure. Closely reflecting variations in N_A with decompression rate, time-integrated nucleation rates peak at different pressures for each series (Fig. 9). The pressure of the maximum nucleation rate decreases as the decompression rate increases. Nucleation rate maxima occur at 5, 26, 45, and 109 MPa, respectively, as decompression rate decreases from 10 to 0·5 MPa h^{-1}.

Average plagioclase growth rates in snapshot samples range from 10^{-6} to 10^{-9} mm s^{-1} (Fig. 10), which is the same range found in previous MSD experiments utilizing intermediate to silicic magmas (Hammer & Rutherford, 2002; Couch *et al.*, 2003*b*). However, each decompression rate is associated with a unique range of G, and the magnitude of internal variation is markedly different for each decompression rate. The slowest decompression series

Table 4: Select analyses of crystalline phases, wt%

Sample	Phase*	SiO_2	TiO_2	Al_2O_3	FeO†	Fe_2O_3	MnO	MgO	CaO	Na_2O	K_2O	An	Ab	Or	K_d
5-1	plag	63·03	n.d.	22·93	n.d.	n.d.	n.d.	n.d.	4·43	8·67	0·68	21·2	75·0	3·9	2·7
5-2	opx	53·28	0·22	0·56	20·06	n.d.	1·80	22·40	1·31	0·00	0·00				
5-2	Na-pyx	46·12	2·06	9·27	13·95	n.d.	0·79	14·07	9·69	2·07	0·41				
5-2	plag	60·39	n.d.	24·73	n.d.	n.d.	n.d.	n.d.	6·48	7·14	0·37	32·7	65·1	2·2	4·6
5-4	opx	53·11	0·22	1·00	19·78	n.d.	1·82	21·92	2·09	0·00	0·02				
5-4	cpx	51·67	0·62	2·20	12·26	n.d.	1·32	14·19	16·77	0·40	0·08				
5-4	plag	60·35	n.d.	24·59	n.d.	n.d.	n.d.	n.d.	6·72	6·74	0·35	34·8	63·1	2·1	3·5
6-1	opx	52·67	0·27	0·88	19·48	n.d.	1·85	21·81	1·76	0·00	0·01				
6-1	cpx	52·27	0·31	1·23	9·90	n.d.	0·95	14·12	20·01	0·32	0·02				
6-1	plag	60·17	n.d.	24·95	n.d.	n.d.	n.d.	n.d.	6·70	7·41	0·33	32·7	65·4	1·9	7·3
6-2	opx	52·92	0·26	0·98	19·37	n.d.	1·89	21·98	2·51	0·01	0·01				
6-2	plag	59·46	n.d.	25·07	n.d.	n.d.	n.d.	n.d.	7·06	7·28	0·34	34·2	63·8	2·0	18·3
7-1	plag	59·24	n.d.	25·19	n.d.	n.d.	n.d.	n.d.	6·86	7·51	0·38	32·8	65·0	2·1	4·1
7-2	opx	53·80	0·19	0·68	18·78	n.d.	1·74	24·22	1·24	0·00	0·00				
7-2	Na-pyx	45·94	2·13	9·16	10·40	n.d.	0·82	15·79	10·83	2·22	0·45				
7-2	cpx	50·00	1·09	3·58	11·08	n.d.	0·87	13·03	19·69	0·43	0·02				
7-2	plag	58·87	n.d.	25·61	n.d.	n.d.	n.d.	n.d.	7·22	7·11	0·34	35·2	62·8	2·0	5·5
7-4	opx	52·96	0·28	0·81	19·34	n.d.	2·12	23·12	1·53	0·00	0·00				
7-4	Na-pyx	46·79	1·81	8·55	11·30	n.d.	0·81	15·73	10·59	2·05	0·36				
7-4	cpx	52·12	0·41	1·57	10·01	n.d.	0·90	14·43	20·11	0·35	0·03				
7-4	plag	59·85	n.d.	24·61	n.d.	n.d.	n.d.	n.d.	6·62	7·30	0·47	32·5	64·8	2·8	4·8
8-1	Na-pyx	45·87	1·78	9·50	9·80	n.d.	0·76	16·46	10·93	2·17	0·44				
8-1	cpx	52·47	0·34	1·22	8·54	n.d.	1·07	14·71	20·35	0·37	0·02				
8-1	plag	60·28	n.d.	24·69	n.d.	n.d.	n.d.	n.d.	6·32	7·71	0·41	30·4	67·2	2·3	7·0
8-3	opx	54·13	0·26	0·70	16·09	n.d.	3·27	24·44	1·26	0·00	0·03				
8-3	plag	59·98	n.d.	24·19	n.d.	n.d.	n.d.	n.d.	6·29	7·62	0·50	30·4	66·7	2·9	7·0
11-1	mgt	0·13	9·37	1·90	37·19	47·87	1·28	0·83	0·05	0·01	0·02				
11-1	ilm	0·06	42·64	0·16	33·44	16·18	1·97	1·64	0·05	0·01	0·02				
11-1	opx	53·47	0·30	0·46	19·48	n.d.	1·87	22·01	1·34	0·01	0·01				
11-1	plag	66·64	n.d.	19·69	n.d.	n.d.	n.d.	n.d.	2·99	7·40	2·03	15·9	71·3	12·8	5·9
12-1	plag	59·58	n.d.	25·38	n.d.	n.d.	n.d.	n.d.	6·83	7·67	0·35	32·3	65·7	2·0	3·1
12-2	plag	58·44	n.d.	23·69	n.d.	n.d.	n.d.	n.d.	6·09	7·09	0·46	31·3	65·9	2·8	3·7
13-1	opx	54·94	0·24	0·69	15·26	n.d.	2·94	25·07	0·93	0·03	0·00				
13-1	plag	62·20	0·02	22·28	0·40	n.d.	0·03	0·02	4·73	7·86	0·84	23·7	71·3	5·0	6·8
13-2	opx	53·55	0·18	0·73	20·26	n.d.	1·78	21·90	1·45	0·02	0·06				
13-2	plag	62·35	n.d.	22·65	n.d.	n.d.	n.d.	n.d.	4·27	8·15	1·68	20·3	70·2	9·5	8·0
13-3	opx	52·63	0·26	0·93	19·98	n.d.	1·88	21·92	1·70	0·00	0·04				
13-3	plag	61·02	n.d.	23·64	n.d.	n.d.	n.d.	n.d.	5·71	7·67	0·63	28·1	68·3	3·7	10·8
14-1	opx	53·03	0·18	0·56	20·24	n.d.	1·88	22·37	1·43	0·01	0·01				
14-1	cpx	51·02	0·52	2·36	11·93	n.d.	1·20	14·33	17·12	0·39	0·04				
14-1	plag	59·96	n.d.	24·77	n.d.	n.d.	n.d.	n.d.	6·48	7·47	0·42	31·6	65·9	2·4	3·4
14-2	opx	52·94	0·28	0·95	19·01	n.d.	1·93	23·23	1·46	0·00	0·00				
14-2	Na-pyx	46·67	1·82	9·20	10·43	n.d.	0·69	15·55	10·66	2·10	0·43				
14-2	cpx	51·31	0·56	2·02	13·76	n.d.	0·38	14·37	17·02	0·33	0·02				
14-2	plag	60·03	n.d.	24·35	n.d.	n.d.	n.d.	n.d.	6·17	7·64	0·43	30·1	67·4	2·5	3·3
15-1	plag	61·58	n.d.	23·90	n.d.	n.d.	n.d.	n.d.	5·79	7·70	0·46	28·6	68·7	2·7	2·8
15-2	Na-pyx	47·08	1·77	8·07	11·77	n.d.	1·04	15·86	9·91	2·03	0·38				
15-2	plag	59·29	n.d.	24·37	n.d.	n.d.	n.d.	n.d.	6·39	7·40	0·42	31·5	66·0	2·5	7·1
15-3	mgt	0·15	6·66	2·28	31·70	54·02	1·87	2·59	0·04	0·01	0·02				

(continued)

Table 4: Continued

Sample	Phase*	SiO_2	TiO_2	Al_2O_3	FeO†	Fe_2O_3	MnO	MgO	CaO	Na_2O	K_2O	An	Ab	Or	K_d
15-3	cpx	50·87	0·94	2·80	13·27	n.d.	0·51	15·24	15·15	0·29	0·01				
15-3	opx	52·48	0·92	4·57	13·77	n.d.	1·94	20·49	3·81	0·62	0·34				
15-3	Na-pyx	45·12	2·04	9·90	11·62	n.d.	0·62	15·01	10·59	2·19	0·46				
15-3	plag	64·60	n.d.	23·62	n.d.	n.d.	n.d.	n.d.	5·32	7·91	0·59	26·2	70·4	3·5	3·9
15-4	Na-pyx	46·11	2·13	9·17	11·54	n.d.	0·70	15·16	10·43	2·16	0·43				
15-4	cpx	52·99	0·35	2·18	10·13	n.d.	1·35	14·95	17·49	0·39	0·12				
15-4	plag	62·47	n.d.	23·08	n.d.	n.d.	n.d.	n.d.	5·02	8·29	0·58	24·2	72·4	3·3	3·5
15-5	plag	60·73	n.d.	24·96	n.d.	n.d.	n.d.	n.d.	6·50	7·37	0·44	31·9	65·5	2·6	3·6
15-6	opx	53·11	0·24	1·15	17·16	n.d.	3·42	23·53	0·92	0·01	0·02				
15-6	plag	60·42	n.d.	24·70	n.d.	n.d.	n.d.	n.d.	6·66	7·56	0·47	31·8	65·5	2·7	6·2
15-7	opx	53·69	0·21	0·63	19·75	n.d.	1·93	22·97	1·24	0·00	0·04				
15-7	Na-pyx	47·47	2·26	9·89	12·04	n.d.	0·74	14·00	9·29	2·54	0·74				
15-7	plag	64·69	n.d.	20·82	n.d.	n.d.	n.d.	n.d.	2·45	7·91	2·45	12·4	72·7	14·8	4·5
16-1	Na-pyx	47·66	1·65	8·90	9·95	n.d.	0·81	15·52	10·92	2·30	0·51				
16-1	cpx	52·12	0·70	2·70	10·15	n.d.	1·07	14·14	18·05	0·62	0·09				
16-1	plag	60·12	n.d.	25·05	n.d.	n.d.	n.d.	n.d.	6·74	7·44	0·39	32·6	65·2	2·2	3·4
16-2	mgt	0·12	8·37	1·92	33·84	51·33	1·67	2·38	0·02	0·04	0·01				
16-2	ilm	0·06	44·87	0·16	30·16	16·49	2·48	4·32	0·03	0·02	0·01				
16-2	opx	54·55	0·21	0·69	18·65	n.d.	1·98	22·85	1·28	0·04	0·00				
16-2	Na-pyx	45·82	2·39	8·74	10·36	n.d.	0·73	15·37	10·67	2·24	0·44				
16-2	plag	61·36	n.d.	24·33	n.d.	n.d.	n.d.	n.d.	5·81	7·55	0·54	28·9	67·9	3·2	4·1
17-3	plag	58·54	0·00	24·90	0·49	n.d.	0·01	0·03	6·96	7·18	0·36	34·2	63·7	2·1	18·3
18-1	mgt	0·11	6·44	2·11	32·05	54·49	1·52	2·37	0·01	0·02	0·02				
18-1	opx	53·99	0·22	0·49	19·19	n.d.	1·82	22·07	1·68	0·01	0·02				
18-1	Na-pyx	46·02	2·63	8·99	11·01	n.d.	0·69	15·10	10·56	2·22	0·50				
18-1	cpx	52·07	0·75	2·59	9·82	n.d.	0·95	14·10	19·01	0·44	0·03				
18-1	plag	59·72	0·04	23·77	0·59	n.d.	0·00	0·02	5·65	7·80	0·51	27·7	69·2	3·0	2·9
18-2	plag	56·91	n.d.	23·98	n.d.	n.d.	n.d.	n.d.	6·05	7·29	0·43	30·6	66·8	2·6	5·7
18-3	plag	60·61	n.d.	24·01	n.d.	n.d.	n.d.	n.d.	6·16	7·37	0·56	30·6	66·1	3·3	11·2
18-4	plag	60·44	n.d.	24·36	n.d.	n.d.	n.d.	n.d.	6·18	7·52	0·45	30·4	67·0	2·6	3·6
18-5	plag	60·19	n.d.	23·39	n.d.	n.d.	n.d.	n.d.	5·24	7·92	0·54	25·9	70·9	3·2	3·3
20-1	plag	58·51	n.d.	23·47	n.d.	n.d.	n.d.	n.d.	5·54	7·62	0·45	27·9	69·4	2·7	3·7
20-2	plag	60·77	n.d.	24·75	n.d.	n.d.	n.d.	n.d.	6·55	7·14	0·47	32·7	64·5	2·8	3·6
20-3	plag	63·36	n.d.	22·15	n.d.	n.d.	n.d.	n.d.	3·78	8·46	1·09	18·5	75·1	6·4	3·8
21-1	plag	59·51	n.d.	24·69	n.d.	n.d.	n.d.	n.d.	6·32	7·19	0·36	32·0	65·8	2·2	4·8
22-1	opx	53·14	0·27	0·57	20·22	n.d.	1·93	21·61	1·37	0·03	0·00				
22-1	cpx	49·89	0·96	3·76	8·39	n.d.	1·09	13·94	20·15	0·55	0·04				
22-1	plag	59·60	0·05	23·03	0·63	n.d.	0·01	0·04	5·60	7·78	0·50	27·6	69·4	2·9	2·1
22-2	mgt	0·29	9·60	3·54	35·32	44·81	1·13	2·31	0·03	0·00	0·09				
22-2	opx	53·32	0·21	1·13	15·91	n.d.	1·94	23·25	2·54	0·05	0·01				
22-2	cpx	48·98	1·13	4·37	9·92	n.d.	1·16	13·13	18·95	0·49	0·05				
22-2	plag	62·40	0·02	22·17	0·53	n.d.	0·00	0·06	4·65	8·17	0·58	23·1	73·5	3·4	2·3
BJ3	plag	59·37	n.d.	23·07	n.d.	n.d.	n.d.	n.d.	5·36	7·30	0·73	27·6	67·9	4·5	7·1

*Phases: plag, most Ab-rich plagioclase analyzed; opx, orthopyroxene; cpx, clinopyroxene; Na-pyx, sodium-rich pyroxene; ilm, ilmenite; mgt, magnetite.
†Iron is listed as total iron, except that in ilm and mgt was converted into FeO and Fe_2O_3 using ILMAT (Lepage, 2003).
n.d., not determined.

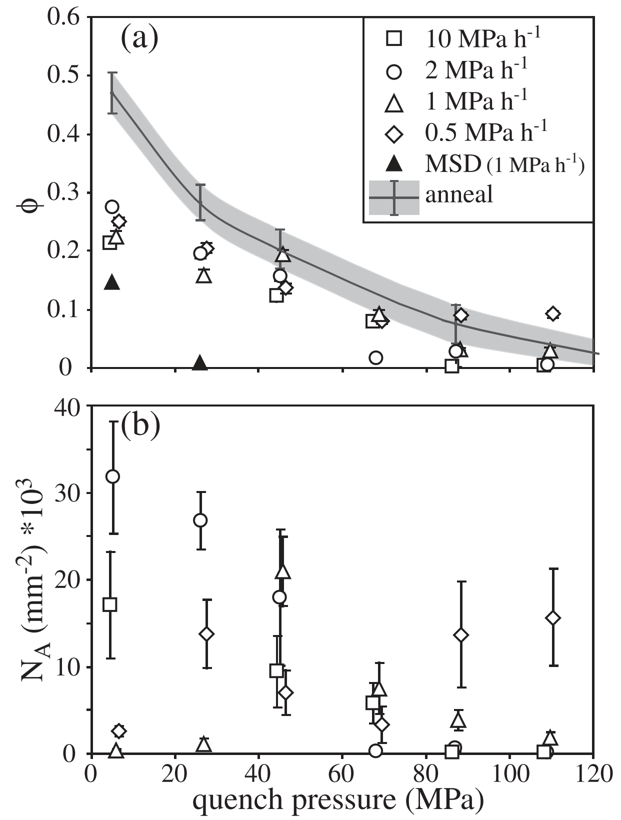

Fig. 7. (a) Volume fraction of plagioclase (ϕ) in each run as a function of decompression rate and quench pressure. The anneal curve was created by averaging all the anneal runs at the given quench pressure and the shading represents the 1σ error of this variation. The 1σ error bars are calculated using the equation of Van der Plas & Tobi (1965) for estimation of point counting errors. Where error bars are not visible they are smaller than the symbol. (b) The number density of plagioclase microlites (N_A) in each sample as a function of decompression rate and quench pressure. The error bars are 1σ values representing variation between BSE images. Each decompression series is offset slightly on the *x*-axis for clarity.

produces *G* values spanning less than one order of magnitude, whereas *G* values from the fastest decompressions vary by more than two orders of magnitude. In the two fastest decompression series, maximum *G* occurs at the highest pressure (109 MPa) and then steadily decreases with decreasing P_f. In contrast, crystal growth rates in the two slower decompression series remain fairly constant throughout decompression.

DISCUSSION

Melt evolution during decompression

Compositions of anneal and snapshot glasses are projected into the haplogranite (Qtz–Ab–Or) ternary diagram using the scheme of Blundy & Cashman (2001; Fig. 11), a tool for tracking liquid lines of descent (LLD) in silicic liquids with ≤1 wt% normative corundum (e.g. Cashman & Blundy, 2000; Hammer & Rutherford, 2002; Couch *et al.*, 2003*b*; Martel & Schmidt, 2003). At each quench pressure, the liquid compositions of the four anneal runs are the same within uncertainty (Fig. 11a). Together, these anneal melts define a trend interpreted to represent the equilibrium liquid line of descent. Between 130 and 45 MPa all of the anneal melts follow a similar trajectory away from the Ab component towards the feldspar–quartz cotectic, consistent with progressive crystallization of feldspar. Between 45 and 5 MPa the anneal trend reaches the cotectic, having saturated with a silica phase, and bends toward the Qtz–Or join. Whereas the position of the 5 MPa quartz–feldspar cotectic in Qtz–Ab–Or haplogranitic melts has not been explicitly determined, the positions of the cotectic between 500 and 50 MPa were determined by Tuttle & Bowen (1958), Luth *et al.* (1964) and Ebadi & Johannes (1991), and the 1 atm (0·1 MPa) cotectic was defined by Brugger *et al.* (2003) using projections of natural rock experimental data into the Qtz–Ab–Or system (projection scheme of Blundy & Cashman, 2001). The 5 MPa anneal runs plot in the approximate location of the interpolated 5 MPa cotectic.

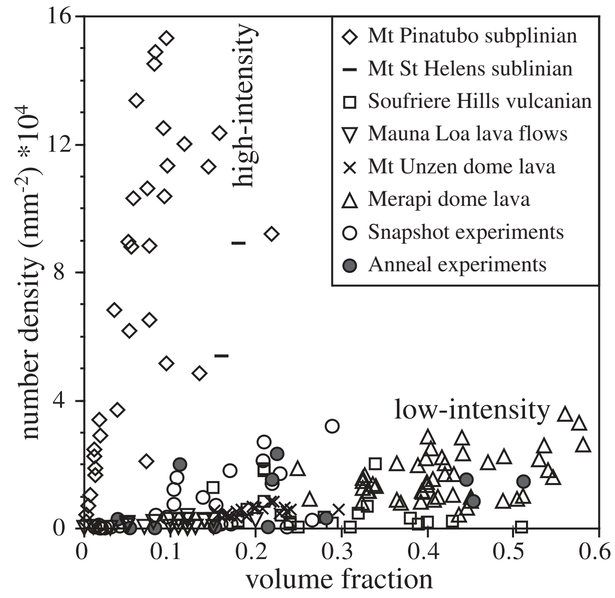

Fig. 8. Textural differences between high-intensity and low-intensity eruptions are displayed on a plot of number density (N_A) vs plagioclase volume fraction (ϕ). Data sources: Pinatubo, Hammer *et al.* (1999); Merapi, Hammer *et al.* (2000); Mount St. Helens, Cashman & McConnell (2005); Soufrière Hills, Clarke *et al.* (2007); Mt Unzen, Noguchi *et al.* (2008); Mauna Loa, Riker *et al.* (2009).

Two snapshot samples containing >1·7 wt% normative corundum, both quenched at 45 MPa, are labeled on the plot but omitted from discussion because they fall outside the compositional range accounted for in the projection

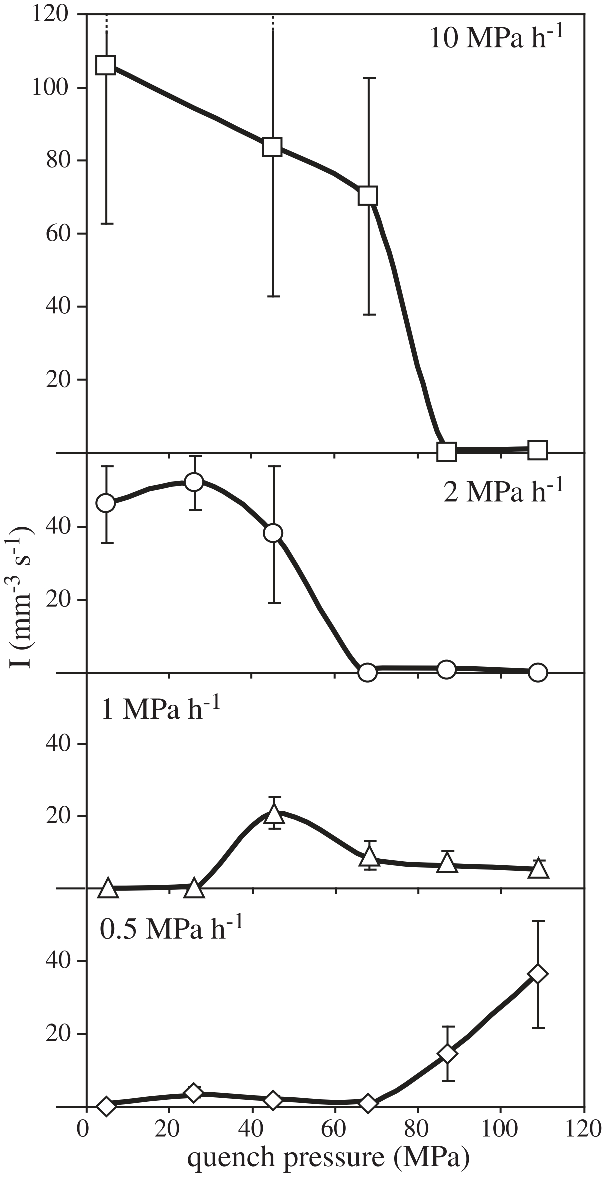

Fig. 9. Nucleation rate (I) of plagioclase microlites in each sample as a function of quench pressure. Error bars are 1σ values.

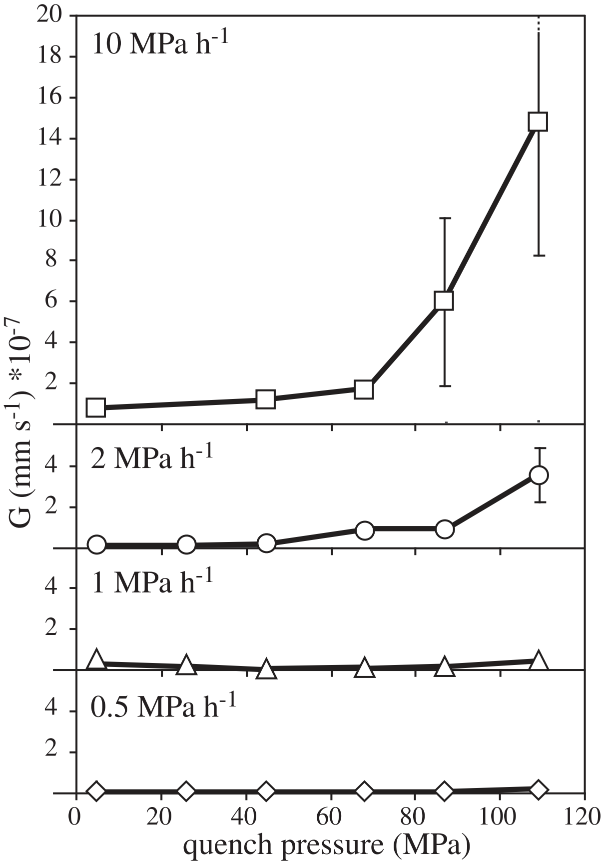

Fig. 10. Growth rate (G) of plagioclase microlites in each sample as a function of quench pressure. Error bars are 1σ values.

scheme. As expected from the glass data, the LLD of snapshot experiments performed at all decompression rates initially tracks with the anneal curve, but deviates appreciably at $P_f \leq 45$ MPa (Fig. 11b–e). Surprisingly, the low-P_f snapshot glass compositions appear to plot on a high-pressure (~500 MPa) quartz–feldspar cotectic, as they are significantly closer to the Qtz–Or join than the equilibrium LLD trend, and they are further from the Qtz apex than any plausible low-pressure cotectic. However, none of the snapshot runs contain a trace of crystalline silica, and so the turn toward the Qtz–Or join is not the result of quartz (or cristobalite) + plagioclase co-crystallization. This low-pressure deflection toward the Qtz–Or join without crystallization of a silica phase has been observed in previous decompression experiments involving silicic melts (Hammer & Rutherford, 2002; Martel & Schmidt, 2003). One possible explanation for this deflection is crystallization of excessively Ca-rich feldspar, which results in a downward bend of the LLD (Fig. 11f). Another possibility is that the deflection is caused by a decrease in the proportion of feldspar in the crystallizing assemblage. That is, although the SiO_2 contents (anhydrous basis) of the 5 MPa snapshot glasses are identical to the SiO_2 contents of 45 MPa glasses, their K_2O contents are higher and Al_2O_3 is unchanged (Fig. 5). For Al_2O_3 to become only moderately compatible in the crystallizing assemblage, another phase must ascend in volumetric dominance. Declining proportionate feldspar contribution could arise from excess orthopyroxene (for example) crystallization, but is more probably due to a declining rate of plagioclase crystallization. Both possibilities may act in concert. As discussed above, snapshot

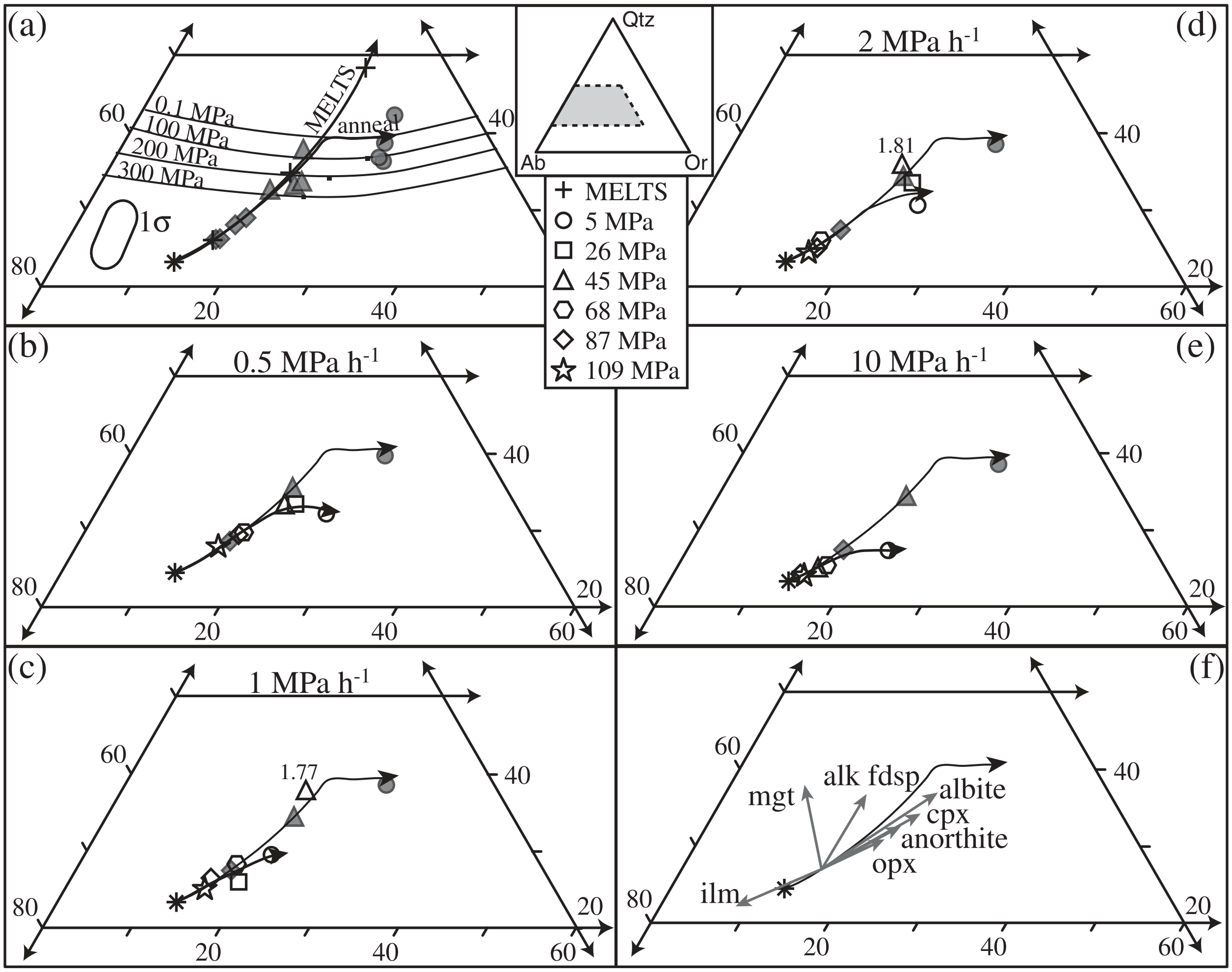

Fig. 11. Projection of snapshot, anneal, and MELTS calculated liquids into the Qz–Ab–Or ternary diagram using the projection scheme of Blundy & Cashman (2001). The dashed quadrilateral in the inset represents the area depicted in (a)–(f). The star (*) in each panel represents the glass composition of the starting material after annealing for $\geq$24 h at 130 MPa and 880°C. The MELTS modeling utilized this glass composition along with 4·33 wt % H_2O, [the saturation value calculated by the water solubility model of Moore *et al.* (1998)], an oxygen fugacity corresponding to NNO + 1, and bulk equilibrium crystallization. (a) Comparisons between MELTS calculated liquids (black crosses) and anneal experiments at 87 MPa (filled diamonds), 45 MPa (filled triangles), and 5 MPa (filled circles) for each decompression series. A liquid line of descent trajectory is shown for MELTS and for the anneal experiments. Quartz–feldspar cotectics and thermal minima are shown for 300, 200, 100, and 0·1 MPa. The 1σ error ellipse for experimental glasses is based on the chemical errors of SiO_2, Na_2O, and K_2O (Table 3) and applies to (a)–(e). (b–e) Snapshot experiments (open symbols) at each quench pressure and estimated snapshot trajectory compared with the anneal liquid line of descent (filled symbols represent the average anneal composition). Two samples contain >1 wt % normative corundum, the maximum abundance accounted for in the projection scheme. The normative corundum abundance in these two samples is labeled in (c) and (d). (f) Given a melt composition lying on the equilibrium liquid line of descent, each arrow represents the trajectory of the melt resulting from crystallization of a particular phase (magnitude of the arrow is not relevant, only direction).

samples consistently contain less feldspar than the corresponding anneal samples, and the discrepancy increases with decreasing P_{f} (Fig. 7a). In addition, snapshot feldspar is on average more Ca-rich than anneal feldspar for a given P_{f} (Fig. 6), as discussed in greater detail below.

The MELTS algorithm (Ghiorso & Sack, 1995; Asimow & Ghiorso, 1998) is widely used to calculate equilibrium phase relations in mafic igneous systems (e.g. Trua *et al.*, 2002; Eason & Sinton, 2006; McCarter *et al.*, 2006; Fowler *et al.*, 2007). Because of a lack of sufficient phase equilibrium data for hydrous multicomponent magmas at pressure <200 MPa, the model is not considered applicable to crystallization of magmas such as andesites, dacites, or rhyolites at crustal conditions. The anneal experiments described here, which we believe represent points along an equilibrium LLD during isothermal decompression, provide an opportunity to assess the predictive ability of MELTS outside its calibration range. Applying the intensive variables of the experiments presented here (880°C, $P_\mathrm{i} = 130$ MPa, $fO_2 = \mathrm{NNO} + 1$), we model crystallization of the H_2O-saturated Aniakchak starting material using bulk equilibrium crystallization and a pressure step-size of 1 MPa. The MELTS calculated LLD closely matches the glass compositions of the anneal samples between 130 and 45 MPa (Fig. 11a). However, at 5 MPa the MELTS liquid overshoots the anneal-derived 5 MPa quartz–feldspar cotectic by *c.* 10 normative wt% Qtz (Fig. 11a), and finally predicts silica saturation at 3 MPa. MELTS also fails to predict formation of apatite, clinopyroxene, and alkali feldspar at any pressure. In summary, MELTS adequately predicts the early stages of melt evolution as a result of isothermal decompression, although it does not generate the observed phase assemblage or low-pressure phase relations.

Crystallization kinetics

The time-invariance of anneal run melt compositions allows utilization of these samples to determine chemical disequilibrium in snapshot experiments. By comparing plagioclase volume fractions in anneal and snapshot runs at the same quench pressure, relative magnitudes of crystal supersaturation ($\Delta\phi$)

$$\Delta\phi = \phi_\mathrm{anneal} - \phi_\mathrm{snapshot} \qquad (3)$$

can be used to evaluate how the magnitude of chemical disequilibrium progressively changes during decompression as a function of decompression rate. For snapshot samples with no pressure-equivalent anneal run, equilibrium plagioclase volume fraction is interpolated from neighboring anneal runs. If a snapshot run and corresponding anneal run contain the same volume of plagioclase, $\Delta\phi = 0$ and they are presumed equally crystalline. For all decompression rates examined, $\Delta\phi$ correlates inversely with quench pressure, and as pressure decreases, $\Delta\phi$ increases at an accelerating rate (Fig. 12a). Quench pressure has a much stronger influence on $\Delta\phi$ than does decompression rate, except at the highest quench pressures where rapidly decompressed samples experience a delay in nucleation of plagioclase, which leads to slightly higher $\Delta\phi$ values. The positive relationship between melt viscosity (calculated using Giordano *et al.*, 2008) and $\Delta\phi$ (Fig. 12a inset) hints at the nature of the control on accumulated driving force. With decreasing P_{H_2O} and thus increasing viscosity, diffusivities of crystal-forming components in the melt decrease and interface reactions become more sluggish.

In agreement with previous studies of crystallization kinetics, growth rate appears to depend on the magnitude of chemical disequilibrium, although the nature of the dependence varies with decompression rate (Fig. 12b; Lofgren, 1980; Kirkpatrick, 1981; Cashman, 1990). With the exception of the 1 MPa h^{-1} series, all decompression rates produce maximum growth rates (G_max) at very low $\Delta\phi$, in agreement with theory (Dowty, 1980; Kirkpatrick, 1981). Importantly, the value of G_max correlates with decompression rate. Fast decompression results in the highest crystal growth rates, and slower decompression causes slower crystal growth (Figs 10 and 12b).

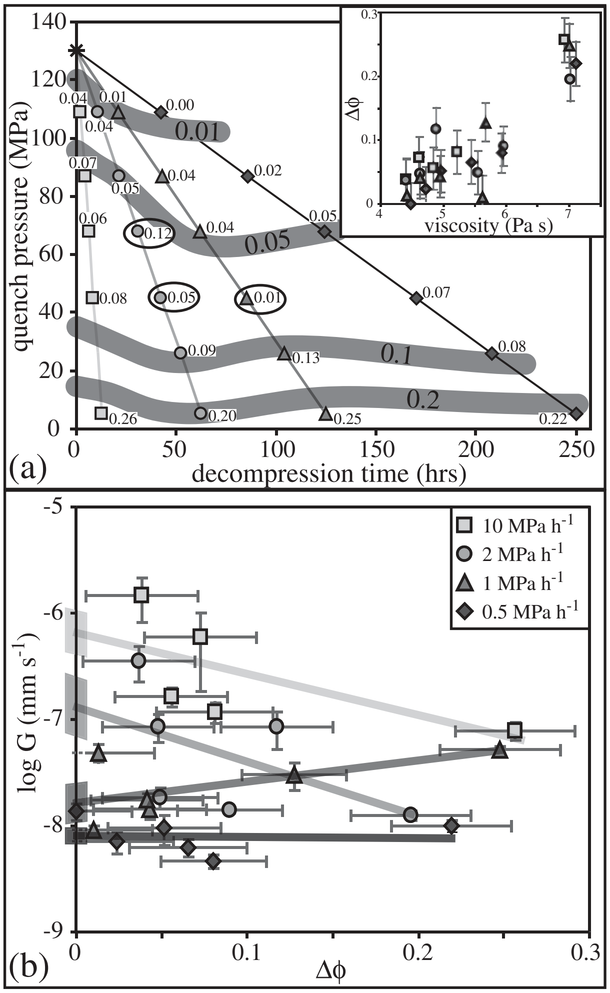

Fig. 12. (a) $\Delta\phi$ contours (wide bands) for values of 0·01, 0·05, 0·1, and 0·2 are drawn by connecting equal interpolated $\Delta\phi$ values in each set of snapshot samples ($\Delta\phi$ values are written next to each experiment). Circled symbols do not satisfy the isograd characterization as drawn. Inset: melt viscosity calculated using the model of Giordano *et al.* (2008) using the melt composition for each sample and its water content at the quench pressure, calculated after Moore *et al.* (1998). (b) Plagioclase growth rate (G) as a function of crystal supersaturation, and the linear best fit for each decompression series. Shaded regions on the *y*-axis represent the linear extrapolation of log G back to $\Delta\phi = 0$, and the heights of the shaded regions reflect scatter in the data.

The preceding estimates of nucleation (I) and growth (G) rates were calculated in the same manner as in all prior experimental decompression studies of crystal

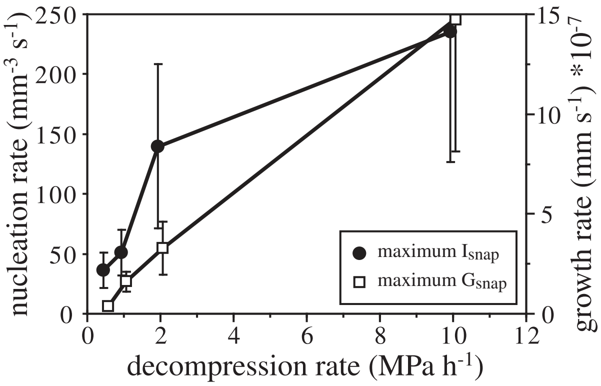

Fig. 13. Maximum values of near-instantaneous nucleation and growth rates (I_{snap} and G_{snap}) plotted as a function of decompression rate. I_{snap} and G_{snap} are calculated using the time duration and change in N_V and S_N, respectively, between neighboring snapshot experiments (see text). Error bars are 1σ values. I_{snap} and G_{snap} are offset slightly on the *x*-axis for clarity.

nucleation and growth rates (e.g. Hammer & Rutherford, 2002; Couch *et al.*, 2003). Although useful, these values incorporate the full decompression duration up to the point of quench and do not reflect instantaneous rates of nucleation and growth. Whereas truly instantaneous rate measurements require continuous knowledge of N_V and S_N variations through time, near-instantaneous nucleation and growth rates can be estimated using neighboring snapshot experiments. Snapshot nucleation rates (I_{snap}) and growth rates (G_{snap}) are calculated using differences in N_V and S_N, respectively, between adjacent snapshot experiments divided by the time spent between the two pressures. For example, G_{snap} between 68 and 45 MPa $= (N_{V\ 45\,MPa} - N_{V\ 68\,MPa})/(\text{time}_{45\,MPa} - \text{time}_{68\,MPa})$. I_{snap} and G_{snap} are still time-averaged values, but they are computed over moving time windows of relatively short duration so they more closely approximate instantaneous rates. To the extent that I and G represent continuous functions of number density and size with respect to quench pressure (sparsely sampled in our experiments; Figs 9 and 10), I_{snap} and G_{snap} are ideally the instantaneous rates of change of these functions. In fact, the maximum I_{snap} and G_{snap} values occur at pressures corresponding to the steepest sloping line segments in Figs 9 and 10, respectively. Values of maximum near-instantaneous nucleation and growth rates are up to three times greater than their time-integrated counterparts. Most importantly, the maximum near-instantaneous I_{snap} and G_{snap} are coherently and monotonically related to decompression rate (Fig. 13). We conclude that magma ascent rate exerts the primary control on instantaneous rates of plagioclase nucleation and growth, presumably because transformation kinetics are intimately linked to the degree of thermodynamic disequilibrium.

Interestingly, all four decompression rates appear to result in the same amount of plagioclase (Fig. 7a) and produce melts with similar compositions (Fig. 5 and Table 2) for any given P_f, despite large differences in the rates of plagioclase nucleation and growth. An inverse relationship between the rates of nucleation and growth (which are individually sensitive to decompression rate) leads to apparent path-independence with respect to overall crystallinity (Fig. 7a). This is consistent with cooling rate studies on calcalkaline and high-K calcalkaline Stromboli lavas, which find similar liquid lines of descent in magmas undergoing very different cooling histories (Conte *et al.*, 2006). Conte *et al.* (2006) concluded that dynamic crystallization conditions have little effect on the residual liquid compositions in multiply saturated assemblages.

MSD vs CD

Magma ascent is very probably fitful during volcanic eruptions, with accelerations and decelerations, irregular pauses and periods of continuous rise (Tuffen *et al.*, 2003; Roman & Cashman, 2006; Scandone *et al.*, 2007; Smith *et al.*, 2007). Examination of the effects of discontinuous magma ascent is a line of experimental inquiry that would be well suited to examination by the programmable pressure variator, as the preceding MSD experimental studies have employed a variety of multi-step methods (Hammer & Rutherford, 2002; Couch *et al.*, 2003*b*; Martel & Schmidt, 2003). In fact, prior experimental work has employed multiple-step decompressions out of technical necessity, with no stated intention of replicating the complexities of a natural process. Although the simple CD scenario we examine is not necessarily more realistic than MSD in principle, the continuous decompression suite provides an essential reference case for any future systematic study of the effects of fitful ascent dynamics on crystal texture.

Textural comparisons between 1 MPa h^{-1} MSD and CD runs indicate that stepwise decompression yields textures correlative with faster decompression than the integrated decompression rate (IDR) would indicate. Plagioclase crystals in CD samples appear faceted, suggesting that interface reaction controlled growth (Fig. 4; Lofgren, 1974; Sunagawa, 1981), typically associated with growth at low effective undercooling. However, these crystals contain occasional melt inclusions and some swallowtail morphologies, demonstrating that they have not undergone near-equilibrium crystallization throughout their formation. In contrast, plagioclase crystals in MSD runs are dominantly hopper and skeletal forms (Fig. 4), indicating a diffusion-limited growth throughout decompression and probably consistently higher effective undercooling (Lofgren, 1974; Corrigan, 1982; Hammer & Rutherford, 2002). Without independent knowledge of the decompression histories of these two samples afforded by the experimental methods, these textural variations would probably be attributed to different magma ascent rates or different closure pressures (Lofgren, 1973; Hammer & Rutherford, 2002).

The mismatch in crystal contents produced in multi-step and continuous decompression at comparable decompression rates has important implications for the volcanological applications of dynamic crystallization experiments. The consistently lower crystallinities produced during these pilot MSD experiments suggest that quantitative determination of the closure pressure of continuously ascended natural magmas using an MSD calibration set could overestimate closure pressure and therefore depth of magma crystallization. As decompression rate increases and step size decreases the differences between CD and MSD experiments will presumably lessen. Further experiments are clearly needed to explore the extent of the MSD–CD textural mismatch with regard to different pressure increments and time steps.

Plagioclase compositions

It is well known from phase equilibrium studies that the An-content of plagioclase decreases continuously with decreasing temperature and P_{H2O} (e.g. Moore & Carmichael, 1998; Couch *et al.*, 2003*a*; Larsen, 2006). Syn-eruptive crystallization, however, is inherently a disequilibrium process. In dynamic systems, the rates of decompression, degassing, and cooling control diffusivities of chemical components in the melt, crystallization rates, and melt composition. In agreement with Castro & Gardner (2008), our results do not support a clear relationship between decompression rate and feldspar composition, although we acknowledge that the small size of elongate crystals formed during rapid decompression precludes quantitative analysis to fully test this assertion. However, there is a robust relationship between the most albitic crystals and P_f, which is revealed when experimental glass and plagioclase compositions are projected into the binary Ab–An system to generate a P_{H2O}–X diagram (Fig. 14). By direct analogy with the T–X plagioclase loop, glass compositions become more Ab-rich with decreasing pressure, and they are always more Ab-rich than the coexisting plagioclase crystals. As previously discussed above, An_{39-43} crystals are present in every run because crystals with this composition formed during the initial dwell period. In anneal samples, the range of plagioclase compositions increases with decreasing pressure; thus we interpret the compositions of the most albitic crystals to reflect growth near the quench pressure. Snapshot experiments also display a general trend of increasingly albitic compositions with decreasing pressure; however, anneal experiments always contain more Ab-rich crystals than snapshot experiments at the same P_f (Fig. 14). This agrees with previous studies reporting plagioclase crystallizing in equilibrium isobaric experiments as more albitic than those forming in MSD experiments at the same P_f (Martel & Schmidt, 2003; Suzuki *et al.*, 2007). Thus, even the most Ab-rich plagioclase crystals in snapshot CD samples do not represent compositional equilibrium crystallization from the coexisting melt despite the fact that high-pressure snapshot experiments contain the equilibrium feldspar abundance (Fig. 7).

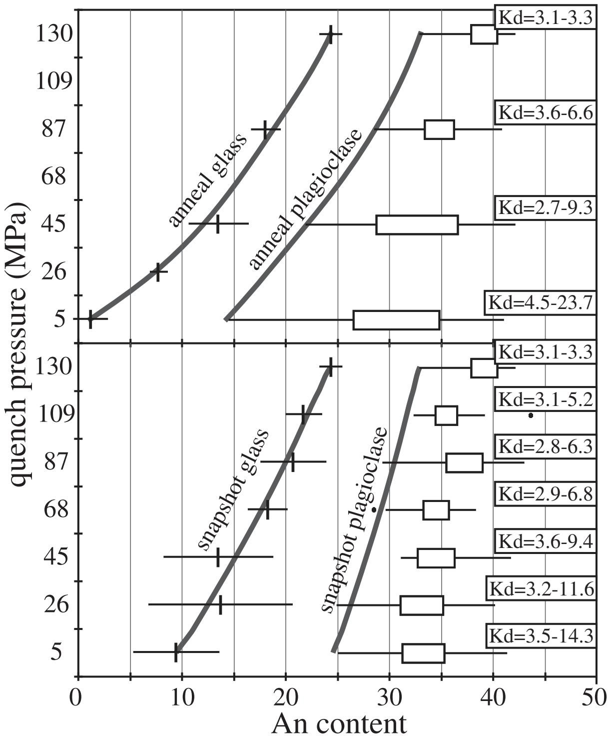

Fig. 14. Albite–Anorthite loop diagram as a function of pressure. The An and Ab component of the melt is determined by using the glass composition at each pressure to calculate the CIPW mole proportion of An and Ab (shown normalized to 100%). All runs at the same quench pressure are averaged together, with error bars representing 1σ variation. For plagioclase compositions the An + Ab components are normalized to 100%. Because of the large variation in plagioclase compositions, all samples quenched at the same pressure are plotted together regardless of decompression rate. The edges of each box represent the upper and lower quartile of all the analyzed plagioclase crystals at a given quench pressure. The left end of the bar and right end of the bar represent the most Ab-rich and most An-rich crystals, respectively. The dots (●) are outlier compositions, defined as greater than 1·5 × IQR (inter-quartile range) from the upper or lower quartile value. The range of K_d values for each quench pressure is shown.

Calcium–sodium partition coefficients for plagioclase are calculated using the molar fraction (X) of CaO and Na_2O in crystals and glass, where

$$K_d = \frac{\left(X_{CaO}^{plag}/X_{Na_2O}^{plag}\right)}{\left(X_{CaO}^{glass}/X_{Na_2O}^{glass}\right)} \quad (4)$$

(Fig. 14, and Supplementary Data Table 1, at http://www.petrology.oxfordjournals.org). Comparisons between plagioclase compositions in experiments and natural rocks have been used to interpret crystallization pressures, magma ascent rates, and the compositional history of co-existing magmas (e.g. Martel *et al.*, 2006; Suzuki *et al.*, 2007). For instance, microlites in the Mount Pelée silicic melt have been interpreted (Martel *et al.*, 2006) to be inherited from a basaltic magma because Ca/Na partition coefficients are greater than five, typically viewed as the upper limit in island-arc magmatic systems (Sisson & Grove, 1993; Martel *et al.*, 1999; Pichavant *et al.*, 2002). However, results of this study show that early formed microlites do not re-equilibrate with the melt over the decompression timescales examined, and thus they are more An-rich than equilibrium plagioclase (Fig. 14). Although it is possible that these micron-scale crystals have extremely thin rims in compositional equilibrium with the melt, no rims are visible in BSE images; and if they do exist, they are too narrow to analyze with a standard electron microprobe. Thus, microlites may retain high partition coefficients as a natural consequence of disequilibrium crystallization during dynamic decompression. Echoing the cautions presented a quarter century ago in the lunar crystallization literature (Grove & Bence, 1979) for mafic minerals, we suggest that phase equilibrium experiments on silicic magmas are inadequate for interpreting hydrous magma ascent processes from crystals formed at disequilibrium.

IMPLICATIONS

It has long been recognized that plagioclase growth rates vary as a function of cooling rate (Walker *et al.*, 1978; Cashman, 1993; Lesher *et al.*, 1999; Conte *et al.*, 2006), and this study suggests that growth rates also depend on decompression rate (Figs 10 and 13). Instantaneous plagioclase growth rates vary by >3 orders of magnitude over the range of decompression rates examined. If ascent rate varies during decompression, which is extremely likely for natural magmas undergoing closed-system degassing, then plagioclase growth rates may likewise vary by several orders of magnitude during ascent (Fig. 10; Hammer & Rutherford, 2002; Couch *et al.*, 2003*b*). This variation has important implications for calculations of magmatic timescales that utilize crystal growth rates, a topic presented in greater detail elsewhere (Brugger & Hammer, 2010).

In agreement with previous studies of decompression-induced crystallization, our results clearly indicate that decompression rate is an important factor controlling crystal morphologies and microlite number densities in volcanic rocks. Examination of the 5 MPa experiments, which most closely represent products of natural decompression during volcanic eruptions, reveals an increasing prominence of disequilibrium morphologies as decompression rate increases (Fig. 2). This trend is consistent with previous studies that map morphological changes with increasing effective undercooling: from compact euhedral, to tabular, then swallowtail and hopper (Lofgren, 1974; Corrigan, 1982; Hammer & Rutherford, 2002). Samples in each decompression series experienced different degrees of undercooling, and of crystal nucleation and growth, and thus had different final microtextures. Faster decompression produces high microlite number densities that record late-stage high instantaneous effective undercooling, whereas lower N_A (Fig. 7b) and the euhedral morphologies of growth-dominated crystallization reflect smaller instantaneous undercooling throughout slow decompression.

Surprisingly, our CD experiments reveal no relationship between N_V and quench pressure, as has been reported for MSD experiments (Hammer & Rutherford, 2002; Couch *et al.*, 2003*b*), and utilized in interpreting natural samples (Cashman & McConnell, 2005; Clarke *et al.*, 2007; Blundy & Cashman, 2008). Also counterintuitive, we find no relationship between decompression rate and plagioclase microlite compositions, glass compositions, or plagioclase volume fractions. Although the snapshot samples are texturally disparate (Fig. 2), and they clearly did not all attain chemical equilibrium (Figs 5, 7, 11, and 14), they do contain approximately equal volumes of plagioclase crystals at each given quench pressure (Fig. 7a). The difference between ϕ in snapshot and anneal experiments increases with continued decompression, indicating declining chemical equilibrium that is remarkably insensitive to decompression rate. Within the range of decompression rates investigated in this study, growth of pre-existing crystals and nucleation of new crystals apparently sustains a given (disequilibrium) proportion of feldspar at each pressure, and samples consistently maintain low, but non-zero, effective undercooling.

Results from decompression experiments are commonly compared with textural characteristics of natural rocks to make interpretations about magma ascent rates (e.g. Rutherford & Hill, 1993; Hammer & Rutherford, 2002; Couch *et al.*, 2003*b*; Nicholis & Rutherford, 2004; Cashman & McConnell, 2005). The well-founded premise of these studies is that decompression rate exerts a first-order control on crystal microtextures. However, our comparisons between continuous and multi-step decompression experiments at an integrated decompression rate of $1\,\mathrm{MPa\,h^{-1}}$ suggest that magma ascent style may also govern crystallization textures to a first order. In fact, within the range of decompression rates studied here, decompression style has a more pronounced effect on crystal number densities and morphologies than decompression rate. Just as magma ascent rates vary widely across volcanic systems, ascent styles probably span a wide range from purely continuous to entirely pulsatory. In addition, the style of magma ascent almost certainly varies between various magmatic systems and perhaps temporally within any given system. Thus, consideration of ascent style in addition to rate will undoubtedly strengthen the interpretive power of experimental studies for constraining natural magma ascent processes. Evaluation of natural textures with the goal of quantitative interpretation of magma ascent rate may only be meaningful using experimentally calibrated systems that are chemically and thermally similar to the test case. Thus, continuous decompression experiments provide an essential reference case for any future systematic study of textures in naturally decompressed magmas. Future work in this field needs to explore textural variations between MSD and CD experiments with a range of pressure- and time-step sizes and with a variety of magma compositions in an effort to better understand how decompression style controls textural characteristics.

ACKNOWLEDGEMENTS

Thanks go to Jessica Larson for supplying the Aniakchak rhyodacite starting material and to Mac Rutherford, Barbara Jean Kahawaii, Lisa Tatsumi-Petrochilos, and Julie Bowles for their help in running several experiments. Also, thanks go to Eric Hellebrand, Mike Garcia, and John Donovan for their assistance with electron microprobe analyses. This paper was significantly improved by constructive reviews by Wendy Bohrson, Caroline Martel, and two anonymous reviewers.

FUNDING

This work was supported by National Science Foundation CAREER award (EAR04-49888 to J.E.H.).

SUPPLEMENTARY DATA

Supplementary data for this paper are available at *Journal of Petrology* online.

REFERENCES

Asimow, P. D. & Ghiorso, M. S. (1998). Algorithmic modifications extending MELTS to calculate subsolidus phase relations. *American Mineralogist* **83**, 1127–1131.

Blundy, J. & Cashman, K. V. (2001). Ascent-driven crystallization of dacite magmas at Mount St Helens, 1980–1986. *Contributions to Mineralogy and Petrology* **140**, 631–650.

Blundy, J. & Cashman, K. V. (2008). Petrologic reconstruction of magmatic system variables and processes. In: Putirka, K. D. & Tepley, F. J., III (eds) *Minerals, Inclusions and Volcanic Processes. Mineralogical Society of America and Geochemical Society, Reviews in Mineralogy and Geochemistry* **69**, 179–239.

Browne, B. L. & Gardner, J. E. (2006). The influence of magma ascent path on the texture, mineralogy, and formation of hornblende reaction rims. *Earth and Planetary Science Letters* **246**, 161–176.

Brugger, C. R. & Hammer, J. E. (2010). Crystal size distribution analysis of plagioclase in experimentally decompressed hydrous rhyodacite magma. *Earth and Planetary Science Letters* (in press).

Brugger, C. R., Johnston, A. D. & Cashman, K. V. (2003). Phase relations in silicic systems at one-atmosphere pressure. *Contributions to Mineralogy and Petrology* **146**, 356–369.

Burnham, C. W. & Davis, N. F. (1971). The role of H_2O in silicate melts: 1. P–V–T relations in the system $NaAlSi_3O_8$–H_2O to 10 kilobars and 1000°C. *American Journal of Science* **270**, 54–79.

Cashman, K. V. (1988). Crystallization of Mount St. Helens 1980–1986 dacite: a quantitative textural approach. *Bulletin of Volcanology* **50**, 194–209.

Cashman, K. V. (1990). Textural constraints on the kinetics of crystallization of igneous rocks. In: Nicholls, J. & Russell, J. K. (eds) *Modern Methods of Igneous Petrology: Understanding Magmatic Processes. Mineralogical Society of America, Reviews in Mineralogy* **24**, 259–314.

Cashman, K. V. (1992). Groundmass crystallization of Mount St. Helens dacite 1980–1986: a tool for interpreting shallow magmatic processes. *Contributions to Mineralogy and Petrology* **109**, 431–449.

Cashman, K. V. (1993). Relationship between plagioclase crystallization and cooling rate in basaltic melts. *Contributions to Mineralogy and Petrology* **113**, 126–142.

Cashman, K. V. & Blundy, J. (2000). Degassing and crystallization of ascending andesite and dacite. *Philosophical Transactions of the Royal Society of London Series A* **358**, 1487–1513.

Cashman, K. V. & McConnell, S. M. (2005). Multiple levels of magma storage during the 1980 summer eruptions of Mount St. Helens, WA. *Bulletin of Volcanology* **68**, 57–75.

Castro, J. M. & Gardner, J. E. (2008). Did magma ascent rate control the explosive–effusive transition at the Inyo volcanic chain, California? *Geology* **36**, 279–282.

Cheng, H. & Lemlich, R. (1983). Errors in measurement of bubble size distribution in foam. *Industrial and Engineering Chemistry Fundamentals* **22**, 105–109.

Clarke, A. B., Stephens, S., Teasdale, R., Sparks, R. S. J. & Diller, K. (2007). Petrologic constraints on the decompression history of magma prior to Vulcanian explosions at the Soufrière Hills volcano, Montserrat. *Journal of Volcanology and Geothermal Research* **161**, 261–274.

Conte, A.M., Perinelli, C. & Trigila, R. (2006). Cooling kinetics experiments on different Stromboli lavas: Effects on crystal morphologies and phases composition. *Journal of Volcanology and Geothermal Research* **155**, 179–200.

Coombs, M. L., Eichelberger, J. C. & Rutherford, M. J. (2003). Experimental and textural constraints on mafic enclave formation in volcanic rocks. *Journal of Volcanology and Geothermal Research* **119**, 125–144.

Corrigan, G. M. (1982). The crystal morphology of plagioclase feldspar produced during isothermal supercooling and constant rate cooling experiments. *Mineralogical Magazine* **46**, 433–439.

Couch, S., Harford, C. L., Sparks, R. S. J. & Carroll, M. R. (2003*a*). Experimental constraints on the conditions of formation of highly calcic plagioclase microlites at Soufrière Hills Volcano, Montserrat. *Journal of Petrology* **44**, 1455–1475.

Couch, S., Sparks, R. S. J. & Carroll, M. R. (2003*b*). The kinetics of degassing-induced crystallization at Soufrière Hills Volcano, Montserrat. *Journal of Petrology* **44**, 1477–1502.

DeHoff, R. T. & Rhines, F. N. (1968). *Quantitative Microscopy*. New York: McGraw–Hill.

Devine, J. D., Gardner, J. E., Brack, H. P., Layne, G. D. & Rutherford, M. J. (1995). Comparison of microanalytical methods for estimating H_2O contents of silicic volcanic glasses. *American Mineralogist* **80**, 319–328.

Dowty, E. (1980). Crystal growth and nucleation theory and the numerical simulation of igneous crystallization. In: Hargraves, R. B. (ed.) *The Physics of Magmatic Processes*. Princeton, pp. 410–485.

Dreher, S. T., Eichelberger, J. C. & Larsen, J. F. (2005). The petrology and geochemistry of the Aniakchak caldera-forming ignimbrite, Aleutian Arc, Alaska. *Journal of Petrology* **46**, 1747–1768.

Eason, D. & Sinton, J. (2006). Origin of high-Al N-MORB by fractional crystallization in the upper mantle beneath the Galapagos spreading center. *Earth and Planetary Science Letters* **252**, 423–436.

Ebadi, A. & Johannes, W. (1991). Beginning of melting and composition of first melts in the system Qz–Ab–Or–H_2O–CO_2. *Contributions to Mineralogy and Petrology* **106**, 286–295.

Eichelberger, J. C. (1995). Silicic volcanism: ascent of viscous magmas from crustal reservoirs. *Annual Review of Earth and Planetary Sciences* **23**, 41–63.

Endo, E. T., Dzurisin, D. & Swanson, D. A. (1990). Geophysical and observational constraints for shallow ascent rates of dacitic magma at Mount St. Helens. In: Ryan, M. P. (ed.) *Magma Transport and Storage*. New York: Wiley, pp. 317–334.

Fokin, V. M., Kalinina, A. M. & Filipovich, V. N. (1981). Nucleation in silicate glasses and effect of preliminary heat treatment on it. *Journal of Crystal Growth* **52**, 115–121.

Fowler, S. J., Spera, F. J., Bohron, W. A., Belkin, H. E. & De Vivo, B. (2007). Phase equilibria constraints on the chemical and physical evolution of the Campanian ignimbrite. *Journal of Petrology* **48**, 459–493.

Gardner, C. A., Cashman, K. V. & Neal, C. A. (1998). Tephra fall deposits from the 1992 eruption of Crater Peak, Alaska: implications of clast textures for eruptive products. *Bulletin of Volcanology* **59**, 537–555.

Gardner, J. E., Rutherford, M., Carey, S. & Sigurdsson, H. (1995). Experimental constraints on pre-eruptive water contents and changing magma storage prior to explosive eruptions of Mount St Helens volcano. *Bulletin of Volcanology* **57**, 1–17.

Gardner, J. E., Hilton, M. & Carroll, M. R. (1999). Experimental constraints on degassing of magma; isothermal bubble growth during continuous decompression from high pressure. *Earth and Planetary Science Letters* **168**, 201–218.

Geschwind, C.-H. & Rutherford, M. J. (1992). Cummingtonite and the evolution of the Mount St. Helens magma system: an experimental study. *Geology* **20**, 1011–1014.

Geschwind, C.-H. & Rutherford, M. J. (1995). Crystallization of microlites during magma ascent: the fluid mechanics of 1980–1986 eruptions at Mount St Helens. *Bulletin of Volcanology* **57**, 356–370.

Ghiorso, M. S. & Sack, R. O. (1995). Chemical mass transfer in magmatic processes. IV. A Revised and internally consistent thermodynamic model for the interpolation and extrapolation of liquid–solid equilibria in magmatic systems at elevated temperatures and pressures. *Contributions to Mineralogy and Petrology* **119**, 197–212.

Giordano, D., Russell, J. K. & Dingwell, D. B. (2008). Viscosity of magmatic liquids: A model. *Earth and Planetary Science Letters* **271**, 123–134.

Grove, T. L. & Bence, A. E. (1979). Crystallization in a multiply saturated basalt magma; an experimental study of Luna 24 ferrobasalt. *Lunar and Planetary Science Conference* **X**, 439–478.

Hammer, J. E. (2004). Crystal nucleation in hydrous rhyolite: Experimental data applied to classical theory. *American Mineralogist* **89**, 1673–1679.

Hammer, J. E. (2008). *Experimental studies of the kinetics and energetics of magma crystallizationz*. In: Putirka, K. D. & Tepley, F. J., III (eds) *Minerals, Inclusions and Volcanic Processes. Mineralogical Society of America and Geochemical Society, Reviews in Mineralogy and Geochemistry* **69**, 9–59.

Hammer, J. E. & Rutherford, M. J. (2002). An experimental study of the kinetics of decompression-induced crystallization in silicic melts. *Journal of Geophysical Research* **197**, 1–23.

Hammer, J. E., Cashman, K. V., Hoblitt, R. P. & Newman, S. (1999). Degassing and microlite crystallization during pre-climactic events of the 1991 eruption of Mt. Pinatubo, Philippines. *Bulletin of Volcanology* **60**, 355–380.

Hammer, J. E., Cashman, K. V. & Voight, B. (2000). Magmatic processes revealed by textural and compositional trends in Merapi dome lavas. *Journal of Volcanology and Geothermal Research* **100**, 165–192.

Hammer, J. E., Rutherford, M. J. & Hildreth, W. (2002). Magma storage prior to the 1912 eruption at Novarupta, Alaska. *Contributions to Mineralogy and Petrology* **144**, 144–162.

Hoblitt, R. P. & Harmon, R. S. (1993). Bimodal density distribution of cryptodome dacite from the 1980 eruption of Mount St. Helens, Washington. *Bulletin of Volcanology* **55**, 421–437.

James, P. F. (1974). Kinetics of crystal nucleation in lithium silicate glasses. *Physics and Chemistry of Glasses* **15**, 95–105.

James, P. F. (1985). Kinetics of crystal nucleation in silicate glasses. *Journal of Non-Crystalline Solids* **73**, 517–540.

Kirkpatrick, R. J. (1981). Kinetics of crystallization of igneous rocks. In: Lasaga, A. C. & Kirkpatrick, R. J. (eds) *Kinetics of Geochemical Processes. Mineralogical Society of America, Reviews in Mineralogy* **8**, 321–398.

Larsen, J. F. (2006). Rhyodacite magma storage conditions prior to the 3430 y BP caldera-forming eruption of Aniakchak volcano, Alaska. *Contributions to Mineralogy and Petrology* **152**, 523–540.

Lees, J. M. & Crosson, R. S. (1989). Tomographic inversion for three-dimensional velocity structure at Mount St. Helens using earthquake data. *Journal of Geophysical Research* **94**, 5716–5728.

Lepage, L. D. (2003). ILMAT: an excel worksheet for ilmenite-magnetite geothermometry and geobarometry. *Computers & Geosciences* **5**, 673–678.

Lesher, C. E., Cashman, K. V. & Mayfield, J. D. (1999). Kinetic controls on crystallization of Tertiary North Atlantic basalt and implications for the emplacement and cooling history of lava at Site 989, Southeast Greenland rifted margin. *Proceedings of the Ocean Drilling Program* **163**, 135–148.

Lofgren, G. E. (1973). Experimental crystallization of synthetic plagioclase at prescribed cooling rates. *EOS Transactions American Geophysical Union* **54**, 482.

Lofgren, G. E. (1974). An experimental study of plagioclase crystal morphology: isothermal crystallization. *American Journal of Science* **274**, 243–273.

Lofgren, G. E. (1980). Experimental studies on the dynamic crystallization of silicate melts. In: Hargraves, R. B. (ed.) *The Physics of Magmatic Processes*. Princeton, NJ: Princeton University Press, pp. 487–551.

Luth, W. C., Jahns, R. H. & Tuttle, O. F. (1964). The granite system at pressures of 4 to 10 kilobars. *Journal of Geophysical Research* **69**, 759–773.

Mangan, M. & Sisson, T. (2000). Delayed, disequilibrium degassing in rhyolite magma: decompression experiments and implications for explosive volcanism. *Earth and Planetary Science Letters* **183**, 441–445.

Martel, C. & Poussineau, S. (2007). Diversity of eruptive styles inferred from the microlites of Mt Pelée andesite (Martinique, Lesser Antilles). *Journal of Volcanology and Geothermal Research* **166**, 233–254.

Martel, C. & Schmidt, B. C. (2003). Decompression experiments as an insight into ascent rates of silicic magmas. *Contributions to Mineralogy and Petrology* **144**, 397–415.

Martel, C., Pichavant, M., Holtz, F., Scaillet, B., Bourdier, J.-L. & Traineau, H. (1999). Effects of fO_2 and H_2O on andesite phase relations between 2 and 4 kbars. *Journal of Geophysical Research* **104**, 29453–29470.

Martel, C., Ali, A. R., Poussineau, S., Gourgaud, A. & Pichavant, M. (2006). Basalt-inherited microlites in silicic magmas: Evidence from Mount Pelée (Martinique, French West Indies). *Geology* **34**, 905–908.

McCarter, R. L., Fodor, R. V. & Trusdell, F. (2006). Perspectives on basaltic magma crystallization and differentiation: Lava-lake blocks erupted at Mauna Loa volcano summit, Hawaii. *Lithos* **90**, 187–213.

Moore, G. & Carmichael, I. S. E. (1998). The hydrous phase equilibria (to 3 kbar) of an andesite and basaltic andesite from western Mexico: constraints on water content and conditions of phenocryst growth. *Contributions to Mineralogy and Petrology* **130**, 304–319.

Moore, G., Vennemann, T. & Carmichael, I. S. E. (1998). An empirical model for the solubility of H_2O in magmas to 3 kilobars. *American Mineralogist* **83**, 36–42.

Morgan, G. B. & London, D. (1996). Optimizing the electron microprobe analysis of hydrous alkali aluminosilicate glasses. *American Mineralogist* **81**, 1176–1185.

Newman, S., Epstein, S. & Stolper, E. (1988). Water, carbon dioxide, and hydrogen isotopes in glasses from the ca. 1340 A.D. eruption of the Mono Craters, California: constraints on degassing phenomena and initial volatile content. *Journal of Volcanology and Geothermal Research* **35**, 75–96.

Nicholis, M. G. & Rutherford, M. J. (2004). Experimental constraints on magma ascent rate for the Crater Flat volcanic zone hawaiite. *Geology* **32**, 489–492.

Nielsen, C. & Sigurdsson, H. (1981). Quantitative methods of electron microprobe analysis of sodium in natural and synthetic glasses. *American Mineralogist* **66**, 547–552.

Noguchi, S., Toramaru, A. & Nakada, S. (2008). Relation between microlite textures and discharge rate during the 1991–1995 eruptions at Unzen, Japan. *Journal of Volcanology and Geothermal Research* **175**, 141–155.

Papale, P., Moretti, R. & Barbato, D. (2006). The compositional dependence of the saturation surface of $H_2O + CO_2$ fluids in silicate melts. *Chemical Geology* **229**, 78–95.

Peterson, T. D. (1996). A refined technique for measuring crystal size distributions in thin section. *Contributions to Mineralogy and Petrology* **124**, 395–405.

Pichavant, M., Martel, C., Bourdier, J.-L. & Scaillet, B. (2002). Physical conditions, structure, and dynamics of a zoned magma chamber: Mount Pelée (Martinique, Lesser Antilles Arc). *Journal of Geophysical Research* **107**(B5), 2093, doi:10.1029/2001JB000315.

Pichavant, M., Costa, F., Burgisser, A., Scaillet, B., Martel, C. & Poussineau, S. (2007). Equilibration scales in silicic to intermediate magmas—Implications for experimental studies. *Journal of Petrology* **48**, 1955–1972.

Reed, S. J. B. (1993). *Electron Microprobe Analysis*. Cambridge: Cambridge University Press.

Riker, J. M., Cashman, K. V., Kauahikaua, J. P. & Montierth, C. H. (2009). The length of channelized lava flows: Insight from the 1859 eruption of Mauna Loa Volcano, Hawai'i. *Journal of Volcanology and Geothermal Research* **183**, 139–156.

Roman, D. C. & Cashman, K. V. (2006). The origin of volcano-tectonic earthquake swarms. *Geology* **34**, 457–460.

Rutherford, M. J. & Devine, J. D. (1997). Changing magma conditions and ascent rates during the Soufrière Hills eruption on Montserrat. *GSA Today* **8**, 1–7.

Rutherford, M. J. & Gardner, J. E. (2000). Rates of magma ascent. In: Sigurdsson, H. S. (ed.) *Encyclopedia of Volcanoes*. San Diego, CA: Academic Press, pp. 207–218.

Rutherford, M. J. & Hill, P. M. (1993). Magma ascent rates from amphibole breakdown: experiments and the 1980–1986 Mount St. Helens eruptions. *Journal of Geophysical Research* **98**, 19667–19685.

Rutherford, M. J., Sigurdsson, H., Carey, S. & Davis, A. (1985). The May 18, 1980 eruption of Mount St. Helens 1. Melt composition and experimental phase equilibria. *Journal of Geophysical Research* **90**, 2929–2947.

Scandone, R. & Malone, S. D. (1985). Magma supply, magma discharge and readjustment of the feeding systems of Mount St. Helens during 1980. *Journal of Volcanology and Geothermal Research* **23**, 239–262.

Scandone, R., Cashman, K. V. & Malone, S. D. (2007). Magma supply, magma ascent and the style of volcanic eruptions. *Earth and Planetary Science Letters* **253**, 513–529.

Sisson, T. W. & Grove, T. L. (1993). Experimental investigations of the role of H_2O in calc-alkaline differentiation and subduction zone magmatism. *Contributions to Mineralogy and Petrology* **113**, 143–166.

Smith, R., Kilburn, C. R. J. & Sammonds, P. R. (2007). Rock fracture as a precursor to lava dome eruptions at Mount St Helens from June 1980 to October 1986. *Bulletin of Volcanology* **69**, 681–693.

Sunagawa, I. (1981). Characteristics of crystal growth in nature as seen from the morphology of mineral crystals. *Bulletin de Minéralogie* **104**, 81–87.

Suzuki, Y., Gardner, J. E. & Larsen, J. F. (2007). Experimental constraints on syneruptive magma ascent related to the phreatomagmatic phase of the 2000AD eruption of Usu volcano, Japan. *Bulletin of Volcanology* **69**, 423–444.

Szramek, L., Gardner, J. E. & Larsen, J. (2006). Degassing and microlite crystallization of basaltic andesite magma erupting at Arenal Volcano, Costa Rica. *Journal of Volcanology and Geothermal Research* **157**, 182–201.

Trua, T., Serri, G., Marani, M., Runzulli, A. & Gamberi, F. (2002). Volcanological and petrological evolution of Marsili Seamount (southern Tyrrhenian Sea). *Journal of Volcanology and Geothermal Research* **114**, 441–464.

Tuffen, H., Dingwell, D. B. & Pinkerton, H. (2003). Repeated fracture and healing of silicic magma generate flow banding and earthquakes? *Geology* **31**, 1089–1092.

Tuttle, O. F. & Bowen, N. L. (1958). *Origin of granite in light of experimental studies in the system* $NaAlSi_3O_8$–$KAlSi_3O_8$–SiO_2–H_2O. *Geological Society of America Memoirs* **74**, 153 p.

Van der Plas, L. & Tobi, A. C. (1965). A chart for judging the reliability of point counting results. *American Journal of Science* **263**, 87–90.

Walker, D., Powell, M. A., Hays, J. F. & Lofgren, G. E. (1978). Dynamic crystallization of a eucrite basalt. *Lunar and Planetary Science Conference* **9**, 1369–1391.

Wilson, L., Sparks, R. S. J. & Walker, G. P. L. (1980). Explosive volcanic eruptions, IV, The control of magma properties and conduit geometry on eruption column behaviour. *Geophysical Journal of the Royal Astronomical Society* **63**, 117–148.

Zhang, Y. & Behrens, H. (2000). H_2O diffusion in rhyolitic melts and glasses. *Chemical Geology* **169**, 243–262.

Zhang, Y., Stolper, E. M. & Wasserburg, G. J. (1991). Diffusion of water in rhyolitic glasses. *Geochimica et Cosmochimica Acta* **55**, 441–456.